

Very High-Energy Gamma-Ray Follow-Up Program Using Neutrino Triggers from IceCube

The IceCube Collaboration:

M. G. Aartsen,² K. Abraham,³⁴ M. Ackermann,⁵² J. Adams,¹⁶ J. A. Aguilar,¹² M. Ahlers,³⁰ M. Ahrens,⁴² D. Altmann,²⁴ K. Andeen,³² T. Anderson,⁴⁸ I. Anseau,¹² G. Anton,²⁴ M. Archinger,³¹ C. Argüelles,¹⁴ J. Auffenberg,¹ S. Axani,¹⁴ X. Bai,⁴⁰ S. W. Barwick,²⁷ V. Baum,³¹ R. Bay,⁷ J. J. Beatty,^{18,19} J. Becker Tjus,¹⁰ K.-H. Becker,⁵¹ S. BenZvi,⁴⁹ D. Berley,¹⁷ E. Bernardini,^{52,*} A. Bernhard,³⁴ D. Z. Besson,²⁸ G. Binder,^{8,7} D. Bindig,⁵¹ M. Bissok,¹ E. Blaufuss,¹⁷ S. Blot,⁵² C. Boehm,⁴² M. Börner,²¹ F. Bos,¹⁰ D. Bose,⁴⁴ S. Böser,³¹ O. Botner,⁵⁰ J. Braun,³⁰ L. Brayeur,¹³ H.-P. Bretz,⁵² S. Bron,²⁵ A. Burgman,⁵⁰ T. Carver,²⁵ M. Casier,¹³ E. Cheung,¹⁷ D. Chirkin,³⁰ A. Christov,²⁵ K. Clark,⁴⁵ L. Classen,³⁵ S. Coenders,³⁴ G. H. Collin,¹⁴ J. M. Conrad,¹⁴ D. F. Cowen,^{48,47} R. Cross,⁴⁹ M. Day,³⁰ J. P. A. M. de André,²² C. De Clercq,¹³ E. del Pino Rosendo,³¹ H. Dembinski,³⁶ S. De Ridder,²⁶ P. Desiati,³⁰ K. D. de Vries,¹³ G. de Wasseige,¹³ M. de With,⁹ T. DeYoung,²² J. C. Díaz-Vélez,³⁰ V. di Lorenzo,³¹ H. Dujmovic,⁴⁴ J. P. Dumm,⁴² M. Dunkman,⁴⁸ B. Eberhardt,³¹ T. Ehrhardt,³¹ B. Eichmann,¹⁰ P. Eller,⁴⁸ S. Euler,⁵⁰ P. A. Evenson,³⁶ S. Fahey,³⁰ A. R. Fazely,⁶ J. Feintzeig,³⁰ J. Felde,¹⁷ K. Filimonov,⁷ C. Finley,⁴² S. Flis,⁴² C.-C. Fösig,³¹ A. Franckowiak,⁵² R. Franke,^{52,*} E. Friedman,¹⁷ T. Fuchs,²¹ T. K. Gaisser,³⁶ J. Gallagher,²⁹ L. Gerhardt,^{8,7} K. Ghorbani,³⁰ W. Giang,²³ L. Gladstone,³⁰ T. Glauch,¹ T. Glüsenkamp,⁵² A. Goldschmidt,⁸ G. Golup,¹³ J. G. Gonzalez,³⁶ D. Grant,²³ Z. Griffith,³⁰ C. Haack,¹ A. Haj Ismail,²⁶ A. Hallgren,⁵⁰ F. Halzen,³⁰ E. Hansen,²⁰ T. Hansmann,¹ K. Hanson,³⁰ D. Hebecker,⁹ D. Heereman,¹² K. Helbing,⁵¹ R. Hellauer,¹⁷ S. Hickford,⁵¹ J. Hignight,²² G. C. Hill,² K. D. Hoffman,¹⁷ R. Hoffmann,⁵¹ K. Holzappel,³⁴ K. Hoshina,^{30,a} F. Huang,⁴⁸ M. Huber,³⁴ K. Hultqvist,⁴² S. In,⁴⁴ A. Ishihara,¹⁵ E. Jacobi,⁵² G. S. Japaridze,⁴ M. Jeong,⁴⁴ K. Jero,³⁰ B. J. P. Jones,¹⁴ M. Jurkovic,³⁴ A. Kappes,³⁵ T. Karg,⁵² A. Karle,³⁰ U. Katz,²⁴ M. Kauer,³⁰ A. Keivani,⁴⁸ J. L. Kelley,³⁰ A. Kheirandish,³⁰ M. Kim,⁴⁴ T. Kintscher,⁵² J. Kiryluk,⁴³ T. Kittler,²⁴ S. R. Klein,^{8,7} G. Kohnen,³³ R. Koirala,³⁶ H. Kolanoski,⁹ R. Konietz,¹ L. Köpke,³¹ C. Kopper,²³ S. Kopper,⁵¹ D. J. Koskinen,²⁰ M. Kowalski,^{9,52} K. Krings,³⁴ M. Kroll,¹⁰ G. Krückl,³¹ C. Krüger,³⁰ J. Kunnen,¹³ S. Kunwar,⁵² N. Kurahashi,³⁹ T. Kuwabara,¹⁵ M. Labare,²⁶ J. L. Lanfranchi,⁴⁸ M. J. Larson,²⁰ F. Lauber,⁵¹ D. Lennarz,²² M. Lesiak-Bzdak,⁴³ M. Leuermann,¹ L. Lu,¹⁵ J. Lünemann,¹³ J. Madsen,⁴¹ G. Maggi,¹³ K. B. M. Mahn,²² S. Mancina,³⁰ M. Mandelartz,¹⁰ R. Maruyama,³⁷ K. Mase,¹⁵ R. Maunu,¹⁷ F. McNally,³⁰ K. Meagher,¹² M. Medici,²⁰ M. Meier,²¹ A. Meli,²⁶ T. Menne,²¹ G. Merino,³⁰

*Corresponding author.,

*Corresponding author.

T. Meures,¹² S. Miarecki,^{8,7} L. Mohrmann,⁵² T. Montaruli,²⁵ M. Moulai,¹⁴ R. Nahnauer,⁵² U. Naumann,⁵¹ G. Neer,²² H. Niederhausen,⁴³ S. C. Nowicki,²³ D. R. Nygren,⁸ A. Obertacke Pollmann,⁵¹ A. Olivas,¹⁷ A. O'Murchadha,¹² T. Palczewski,⁴⁶ H. Pandya,³⁶ D. V. Pankova,⁴⁸ P. Peiffer,³¹ Ö. Penek,¹ J. A. Pepper,⁴⁶ C. Pérez de los Heros,⁵⁰ D. Pieloth,²¹ E. Pinat,¹² P. B. Price,⁷ G. T. Przybylski,⁸ M. Quinnan,⁴⁸ C. Raab,¹² L. Rädcl,¹ M. Rameez,²⁰ K. Rawlins,³ R. Reimann,¹ B. Relethford,³⁹ M. Relich,¹⁵ E. Resconi,³⁴ W. Rhode,²¹ M. Richman,³⁹ B. Riedel,²³ S. Robertson,² M. Rongen,¹ C. Rott,⁴⁴ T. Ruhe,²¹ D. Ryckbosch,²⁶ D. Rysewyk,²² L. Sabbatini,³⁰ S. E. Sanchez Herrera,²³ A. Sandrock,²¹ J. Sandroos,³¹ S. Sarkar,^{20,38} K. Satalecka,⁵² P. Schlunder,²¹ T. Schmidt,¹⁷ S. Schoenen,¹ S. Schöneberg,¹⁰ L. Schumacher,¹ D. Seckel,³⁶ S. Seunarine,⁴¹ D. Soldin,⁵¹ M. Song,¹⁷ G. M. Spiczak,⁴¹ C. Spiering,⁵² T. Stanev,³⁶ A. Stasik,⁵² J. Stettner,¹ A. Steuer,³¹ T. Stezelberger,⁸ R. G. Stokstad,⁸ A. Stöbl,⁵² R. Ström,⁵⁰ N. L. Strotjohann,⁵² G. W. Sullivan,¹⁷ M. Sutherland,¹⁸ H. Taavola,⁵⁰ I. Taboada,⁵ J. Tatar,^{8,7} F. Tenholt,¹⁰ S. Ter-Antonyan,⁶ A. Terliuk,⁵² G. Tešić,⁴⁸ S. Tilav,³⁶ P. A. Toale,⁴⁶ M. N. Tobin,³⁰ S. Toscano,¹³ D. Tosi,³⁰ M. Tselengidou,²⁴ A. Turcati,³⁴ E. Unger,⁵⁰ M. Usner,⁵² J. Vandenbroucke,³⁰ N. van Eijndhoven,¹³ S. Vanheule,²⁶ M. van Rossem,³⁰ J. van Santen,⁵² J. Veenkamp,³⁴ M. Vehring,¹ M. Voge,¹¹ E. Vogel,¹ M. Vraeghe,²⁶ C. Walck,⁴² A. Wallace,² M. Wallraff,¹ N. Wandkowsky,³⁰ Ch. Weaver,²³ M. J. Weiss,⁴⁸ C. Wendt,³⁰ S. Westerhoff,³⁰ B. J. Whelan,² S. Wickmann,¹ K. Wiebe,³¹ C. H. Wiebusch,¹ L. Wille,³⁰ D. R. Williams,⁴⁶ L. Wills,³⁹ M. Wolf,⁴² T. R. Wood,²³ E. Woolsey,²³ K. Woschnagg,⁷ D. L. Xu,³⁰ X. W. Xu,⁶ Y. Xu,⁴³ J. P. Yanez,⁵² G. Yodh,²⁷ S. Yoshida,¹⁵ and M. Zoll⁴² and M. Zoll⁴⁰

The MAGIC Collaboration:

M. L. Ahnen,^{51a} S. Ansoldi,^{52a} L. A. Antonelli,⁵³ P. Antoranz,⁵⁴ A. Babic,⁵⁵ B. Banerjee,⁵⁶ P. Bangale,⁵⁷ U. Barres de Almeida,^{57,72} J. A. Barrio,⁵⁸ J. Becerra González,^{59,73} W. Bednarek,⁶⁰ E. Bernardini,^{52,9} A. Berti,^{52a,74} B. Biasuzzi,^{52a} A. Biland,^{51a} O. Blanch,⁶¹ S. Bonnefoy,⁵⁸ G. Bonnoli,⁵³ F. Borracci,⁵⁷ T. Bretz,^{62,75} S. Buson,⁶³ A. Carosi,⁵³ A. Chatterjee,⁵⁶ R. Clavero,⁵⁹ P. Colin,⁵⁷ E. Colombo,⁵⁹ J. L. Contreras,⁵⁸ J. Cortina,⁶¹ S. Covino,⁵³ P. Da Vela,⁵⁴ F. Dazzi,⁵⁷ A. De Angelis,⁶³ B. De Lotto,^{52a} E. de Oña Wilhelmi,⁶⁴ F. Di Pierro,⁵³ M. Doert,²¹ A. Domínguez,⁵⁸ D. Dominis Prester,⁵⁵ D. Dorner,⁶² M. Doro,⁶³ S. Einecke,²¹ D. Eisenacher Glawion,⁶² D. Elsaesser,²¹ M. Engelkemeier,²¹ V. Fallah Ramazani,⁶⁵ A. Fernández-Barral,⁶¹ D. Fidalgo,⁵⁸ M. V. Fonseca,⁵⁸ L. Font,⁶⁶ K. Frantzen,²¹ C. Fruck,⁵⁷ D. Galindo,⁶⁷ R. J. García López,⁵⁹ M. Garczarczyk,⁵² D. Garrido Terrats,⁶⁶ M. Gaug,⁶⁶ P. Giammaria,⁵³ N. Godinović,⁵⁵ A. González Muñoz,⁶¹ D. Góra,^{52,9,*} D. Guberman,⁶¹ D. Hadasch,⁶⁸ A. Hahn,⁵⁷ Y. Hanabata,⁶⁸ M. Hayashida,⁶⁸ J. Herrera,⁵⁹ J. Hose,⁵⁷ D. Hrupec,⁵⁵ G. Hughes,^{51a} W. Idec,⁶⁰ K. Kodani,⁶⁸ Y. Konno,⁶⁸ H. Kubo,⁶⁸ J. Kushida,⁶⁸ A. La Barbera,⁵³ D. Lelas,⁵⁵ E. Lindfors,⁶⁵ S. Lombardi,⁵³ F. Longo,^{52a,74} M. López,⁵⁸ R. López-Coto,^{61,76} P. Majumdar,⁵⁶ M. Makariev,⁶⁹ K. Mallot,⁵² G. Maneva,⁶⁹ M. Manganaro,⁵⁹ K. Mannheim,⁶² L. Maraschi,⁵³ B. Marcote,⁶⁷ M. Mariotti,⁶³ M. Martínez,⁶¹ D. Mazin,^{57,77} U. Menzel,⁵⁷ J. M. Miranda,⁵⁴ R. Mirzoyan,⁵⁷ A. Moralejo,⁶¹

*Corresponding author.

E. Moretti,⁵⁷ D. Nakajima,⁶⁸ V. Neustroev,⁶⁵ A. Niedzwiecki,⁶⁰ M. Nievas Rosillo,⁵⁸
K. Nilsson,^{65,78} K. Nishijima,⁶⁸ K. Noda,⁵⁷ L. Nogués,⁶¹ A. Overkemping,²¹ S. Paiano,⁶³
J. Palacio,⁶¹ M. Palatiello,^{52a} D. Paneque,⁵⁷ R. Paoletti,⁵⁴ J. M. Paredes,⁶⁷
X. Paredes-Fortuny,⁶⁷ G. Pedalletti,⁵² M. Peresano,^{52a} L. Perri,⁵³ M. Persic,^{52,79}
J. Poutanen,⁶⁵ P. G. Prada Moroni,⁷⁰ E. Prandini,^{51a,80} I. Puljak,⁵⁵ I. Reichardt,⁶³
W. Rhode,²¹ M. Ribó,⁶⁷ J. Rico,⁶¹ J. Rodriguez Garcia,⁵⁷ T. Saito,⁶⁸ K. Satalecka,⁵²
S. Schroeder,²¹ C. Schultz,⁶³ T. Schweizer,⁵⁷ A. Sillanpää,⁶⁵ J. Sitarek,⁶⁰ I. Snidaric,⁵⁵
D. Sobczynska,⁶⁰ A. Stamerra,⁵³ T. Steinbring,⁶² M. Strzys,⁵⁷ T. Surić,⁵⁵ L. Takalo,⁶⁵
F. Tavecchio,⁵³ P. Temnikov,⁶⁹ T. Terzić,⁵⁵ D. Tescaro,⁶⁴ M. Teshima,^{57,77} J. Thaele,²¹
D. F. Torres,⁷¹ T. Toyama,⁵⁷ A. Treves,⁵² G. Vanzo,⁵⁹ V. Verguilov,⁶⁹ I. Vovk,⁵⁷ J. E. Ward,⁶¹
M. Will,⁵⁹ M. H. Wu,⁶⁴ R. Zanin,^{67,76}

The VERITAS Collaboration:

A. U. Abeysekara,⁸¹ S. Archambault,⁸² A. Archer,⁸³ W. Benbow,⁸⁴ R. Bird,⁸⁵
E. Bourbeau,⁸² M. Buchovecky,⁸⁵ V. Bugaev,⁸³ K. Byrum,⁸⁶ J. V Cardenzana,⁸⁷
M. Cerruti,⁸⁴ L. Ciupik,⁸⁸ M. P. Connolly,⁸⁹ W. Cui,^{90,91} H. J. Dickinson,⁸⁷ J. Dumm,⁹²
J. D. Eisch,⁸⁷ M. Errando,⁸³ A. Falcone,⁹³ Q. Feng,⁸² J. P. Finley,⁹⁰ H. Fleischhack,⁹⁴
A. Flinders,⁸¹ L. Fortson,⁹² A. Furniss,⁹⁵ G. H. Gillanders,⁸⁹ S. Griffin,⁸² J. Grube,⁸⁸
M. Hütten,⁹⁴ N. Håkansson,⁹⁶ O. Hervet,⁹⁷ J. Holder,⁹⁸ T. B. Humensky,⁹⁹
C. A. Johnson,⁹⁷ P. Kaaret,¹⁰⁰ P. Kar,⁸¹ N. Kelley-Hoskins,⁹⁴ M. Kertzman,¹⁰¹ D. Kieda,⁸¹
M. Krause,⁹⁴ F. Krennrich,⁸⁷ S. Kumar,⁹⁸ M. J. Lang,⁸⁹ G. Maier,⁹⁴ S. McArthur,⁹⁰
A. McCann,⁸² P. Moriarty,⁸⁹ R. Mukherjee,¹⁰² T. Nguyen,¹⁰³ D. Nieto,⁹⁹ S. O'Brien,¹⁰⁴
R. A. Ong,⁸⁵ A. N. Otte,¹⁰³ N. Park,¹⁰⁵ M. Pohl,^{96,94} A. Popkow,⁸⁵ E. Pueschel,¹⁰⁴
J. Quinn,¹⁰⁴ K. Ragan,⁸² P. T. Reynolds,¹⁰⁶ G. T. Richards,¹⁰³ E. Roache,⁸⁴ C. Rulten,⁹²
I. Sadeh,⁹⁴ M. Santander,¹⁰² G. H. Sembroski,⁹⁰ K. Shahinyan,⁹² D. Staszak,¹⁰⁵
I. Telezhinsky,^{96,94} J. V. Tucci,⁹⁰ J. Tyler,⁸² S. P. Wakely,¹⁰⁵ A. Weinstein,⁸⁷ P. Wilcox,¹⁰⁰
A. Wilhelm,^{96,94} D. A. Williams,⁹⁷ B. Zitzer.⁸²

¹*III. Physikalisches Institut, RWTH Aachen University, D-52056 Aachen, Germany*

²*Department of Physics, University of Adelaide, Adelaide, 5005, Australia*

³*Dept. of Physics and Astronomy, University of Alaska Anchorage, 3211 Providence Dr., Anchorage, AK 99508, USA*

⁴*CTSPS, Clark-Atlanta University, Atlanta, GA 30314, USA*

⁵*School of Physics and Center for Relativistic Astrophysics, Georgia Institute of Technology, Atlanta, GA 30332, USA*

⁶*Dept. of Physics, Southern University, Baton Rouge, LA 70813, USA*

⁷*Dept. of Physics, University of California, Berkeley, CA 94720, USA*

⁸*Lawrence Berkeley National Laboratory, Berkeley, CA 94720, USA*

⁹*Institut für Physik, Humboldt-Universität zu Berlin, D-12489 Berlin, Germany*

¹⁰*Fakultät für Physik & Astronomie, Ruhr-Universität Bochum, D-44780 Bochum, Germany*

¹¹*Physikalisches Institut, Universität Bonn, Nussallee 12, D-53115 Bonn, Germany*

¹²*Université Libre de Bruxelles, Science Faculty CP230, B-1050 Brussels, Belgium*

¹³*Vrije Universiteit Brussel, Dienst ELEM, B-1050 Brussels, Belgium*

¹⁴*Dept. of Physics, Massachusetts Institute of Technology, Cambridge, MA 02139, USA*

- ¹⁵*Dept. of Physics and Institute for Global Prominent Research, Chiba University, Chiba 263-8522, Japan*
- ¹⁶*Dept. of Physics and Astronomy, University of Canterbury, Private Bag 4800, Christchurch, New Zealand*
- ¹⁷*Dept. of Physics, University of Maryland, College Park, MD 20742, USA*
- ¹⁸*Dept. of Physics and Center for Cosmology and Astro-Particle Physics, Ohio State University, Columbus, OH 43210, USA*
- ¹⁹*Dept. of Astronomy, Ohio State University, Columbus, OH 43210, USA*
- ²⁰*Niels Bohr Institute, University of Copenhagen, DK-2100 Copenhagen, Denmark*
- ²¹*Dept. of Physics, TU Dortmund University, D-44221 Dortmund, Germany*
- ²²*Dept. of Physics and Astronomy, Michigan State University, East Lansing, MI 48824, USA*
- ²³*Dept. of Physics, University of Alberta, Edmonton, Alberta, Canada T6G 2E1*
- ²⁴*Erlangen Centre for Astroparticle Physics, Friedrich-Alexander-Universität Erlangen-Nürnberg, D-91058 Erlangen, Germany*
- ²⁵*Département de physique nucléaire et corpusculaire, Université de Genève, CH-1211 Genève, Switzerland*
- ²⁶*Dept. of Physics and Astronomy, University of Gent, B-9000 Gent, Belgium*
- ²⁷*Dept. of Physics and Astronomy, University of California, Irvine, CA 92697, USA*
- ²⁸*Dept. of Physics and Astronomy, University of Kansas, Lawrence, KS 66045, USA*
- ²⁹*Dept. of Astronomy, University of Wisconsin, Madison, WI 53706, USA*
- ³⁰*Dept. of Physics and Wisconsin IceCube Particle Astrophysics Center, University of Wisconsin, Madison, WI 53706, USA*
- ³¹*Institute of Physics, University of Mainz, Staudinger Weg 7, D-55099 Mainz, Germany*
- ³²*Department of Physics, Marquette University, Milwaukee, WI, 53201, USA*
- ³³*Université de Mons, 7000 Mons, Belgium*
- ³⁴*Physik-department, Technische Universität München, D-85748 Garching, Germany*
- ³⁵*Institut für Kernphysik, Westfälische Wilhelms-Universität Münster, D-48149 Münster, Germany*
- ³⁶*Bartol Research Institute and Dept. of Physics and Astronomy, University of Delaware, Newark, DE 19716, USA*
- ³⁷*Dept. of Physics, Yale University, New Haven, CT 06520, USA*
- ³⁸*Dept. of Physics, University of Oxford, 1 Keble Road, Oxford OX1 3NP, UK*
- ³⁹*Dept. of Physics, Drexel University, 3141 Chestnut Street, Philadelphia, PA 19104, USA*
- ⁴⁰*Physics Department, South Dakota School of Mines and Technology, Rapid City, SD 57701, USA*
- ⁴¹*Dept. of Physics, University of Wisconsin, River Falls, WI 54022, USA*
- ⁴²*Oskar Klein Centre and Dept. of Physics, Stockholm University, SE-10691 Stockholm, Sweden*
- ⁴³*Dept. of Physics and Astronomy, Stony Brook University, Stony Brook, NY 11794-3800, USA*
- ⁴⁴*Dept. of Physics, Sungkyunkwan University, Suwon 440-746, Korea*
- ⁴⁵*Dept. of Physics, University of Toronto, Toronto, Ontario, Canada, M5S 1A7*
- ⁴⁶*Dept. of Physics and Astronomy, University of Alabama, Tuscaloosa, AL 35487, USA*
- ⁴⁷*Dept. of Astronomy and Astrophysics, Pennsylvania State University, University Park, PA 16802, USA*
- ⁴⁸*Dept. of Physics, Pennsylvania State University, University Park, PA 16802, USA*
- ⁴⁹*Dept. of Physics and Astronomy, University of Rochester, Rochester, NY 14627, USA*
- ⁵⁰*Dept. of Physics and Astronomy, Uppsala University, Box 516, S-75120 Uppsala, Sweden*
- ⁵¹*Dept. of Physics, University of Wuppertal, D-42119 Wuppertal, Germany*
- ⁵²*DESY, D-15735 Zeuthen, Germany*
- ^a*Earthquake Research Institute, University of Tokyo, Bunkyo, Tokyo 113-0032, Japan*
- ^{51a}*ETH Zurich, CH-8093 Zurich, Switzerland*

- ^{52a} *Università di Udine, and INFN Trieste, I-33100 Udine, Italy*
- ⁵³ *INAF National Institute for Astrophysics, I-00136 Rome, Italy*
- ⁵⁴ *Università di Siena, and INFN Pisa, I-53100 Siena, Italy*
- ⁵⁵ *Croatian MAGIC Consortium, Rudjer Boskovic Institute, University of Rijeka, University of Split and University of Zagreb, Croatia*
- ⁵⁶ *Saha Institute of Nuclear Physics, 1/AF Bidhannagar, Salt Lake, Sector-1, Kolkata 700064, India*
- ⁵⁷ *Max-Planck-Institut für Physik, D-80805 München, Germany*
- ⁵⁸ *Universidad Complutense, E-28040 Madrid, Spain*
- ⁵⁹ *Inst. de Astrofísica de Canarias, E-38200 La Laguna, Tenerife, Spain; Universidad de La Laguna, Dpto. Astrofísica, E-38206 La Laguna, Tenerife, Spain*
- ⁶⁰ *University of Łódź, PL-90236 Lodz, Poland*
- ⁶¹ *Institut de Física d'Altes Energies (IFAE), The Barcelona Institute of Science and Technology, Campus UAB, 08193 Bellaterra (Barcelona), Spain*
- ⁶² *Universität Würzburg, D-97074 Würzburg, Germany*
- ⁶³ *Università di Padova and INFN, I-35131 Padova, Italy*
- ⁶⁴ *Institute for Space Sciences (CSIC/IEEC), E-08193 Barcelona, Spain*
- ⁶⁵ *Finnish MAGIC Consortium, Tuorla Observatory, University of Turku and Astronomy Division, University of Oulu, Finland*
- ⁶⁶ *Unitat de Física de les Radiacions, Departament de Física, and CERES-IEEC, Universitat Autònoma de Barcelona, E-08193 Bellaterra, Spain*
- ⁶⁷ *Universitat de Barcelona, ICC, IEEC-UB, E-08028 Barcelona, Spain*
- ⁶⁸ *Japanese MAGIC Consortium, ICRR, The University of Tokyo, Department of Physics and Hakubi Center, Kyoto University, Tokai University, The University of Tokushima, KEK, Japan*
- ⁶⁹ *Inst. for Nucl. Research and Nucl. Energy, BG-1784 Sofia, Bulgaria*
- ⁷⁰ *Università di Pisa, and INFN Pisa, I-56126 Pisa, Italy*
- ⁷¹ *ICREA and Institute for Space Sciences (CSIC/IEEC), E-08193 Barcelona, Spain*
- ⁷² *now at Centro Brasileiro de Pesquisas Físicas (CBPF/MCTI), R. Dr. Xavier Sigaud, 150 - Urca, Rio de Janeiro - RJ, 22290-180, Brazil*
- ⁷³ *now at NASA Goddard Space Flight Center, Greenbelt, MD 20771, USA and Department of Physics and Department of Astronomy, University of Maryland, College Park, MD 20742, USA*
- ⁷⁴ *also at University of Trieste*
- ⁷⁵ *now at Ecole polytechnique fédérale de Lausanne (EPFL), Lausanne, Switzerland*
- ⁷⁶ *now at Max-Planck-Institut für Kernphysik, P.O. Box 103980, D 69029 Heidelberg, Germany*
- ⁷⁷ *also at Japanese MAGIC Consortium*
- ⁷⁸ *now at Finnish Centre for Astronomy with ESO (FINCA), Turku, Finland*
- ⁷⁹ *also at INAF-Trieste and Dept. of Physics & Astronomy, University of Bologna*
- ⁸⁰ *also at ISDC - Science Data Center for Astrophysics, 1290, Versoix (Geneva)*
- ⁸¹ *Department of Physics and Astronomy, University of Utah, Salt Lake City, UT 84112, USA*
- ⁸² *Physics Department, McGill University, Montreal, QC H3A 2T8, Canada*
- ⁸³ *Department of Physics, Washington University, St. Louis, MO 63130, USA*
- ⁸⁴ *Fred Lawrence Whipple Observatory, Harvard-Smithsonian Center for Astrophysics, Amado, AZ 85645, USA*
- ⁸⁵ *Department of Physics and Astronomy, University of California, Los Angeles, CA 90095, USA*
- ⁸⁶ *Argonne National Laboratory, 9700 S. Cass Avenue, Argonne, IL 60439, USA*
- ⁸⁷ *Department of Physics and Astronomy, Iowa State University, Ames, IA 50011, USA*

- ⁸⁸*Astronomy Department, Adler Planetarium and Astronomy Museum, Chicago, IL 60605, USA*
- ⁸⁹*School of Physics, National University of Ireland Galway, University Road, Galway, Ireland*
- ⁹⁰*Department of Physics and Astronomy, Purdue University, West Lafayette, IN 47907, USA*
- ⁹¹*Department of Physics and Center for Astrophysics, Tsinghua University, Beijing 100084, China.*
- ⁹²*School of Physics and Astronomy, University of Minnesota, Minneapolis, MN 55455, USA*
- ⁹³*Department of Astronomy and Astrophysics, 525 Davey Lab, Pennsylvania State University, University Park, PA 16802, USA*
- ⁹⁴*DESY, Platanenallee 6, 15738 Zeuthen, Germany*
- ⁹⁵*Department of Physics, California State University - East Bay, Hayward, CA 94542, USA*
- ⁹⁶*Institute of Physics and Astronomy, University of Potsdam, 14476 Potsdam-Golm, Germany*
- ⁹⁷*Santa Cruz Institute for Particle Physics and Department of Physics, University of California, Santa Cruz, CA 95064, USA*
- ⁹⁸*Department of Physics and Astronomy and the Bartol Research Institute, University of Delaware, Newark, DE 19716, USA*
- ⁹⁹*Physics Department, Columbia University, New York, NY 10027, USA*
- ¹⁰⁰*Department of Physics and Astronomy, University of Iowa, Van Allen Hall, Iowa City, IA 52242, USA*
- ¹⁰¹*Department of Physics and Astronomy, DePauw University, Greencastle, IN 46135-0037, USA*
- ¹⁰²*Department of Physics and Astronomy, Barnard College, Columbia University, NY 10027, USA*
- ¹⁰³*School of Physics and Center for Relativistic Astrophysics, Georgia Institute of Technology, 837 State Street NW, Atlanta, GA 30332-0430*
- ¹⁰⁴*School of Physics, University College Dublin, Belfield, Dublin 4, Ireland*
- ¹⁰⁵*Enrico Fermi Institute, University of Chicago, Chicago, IL 60637, USA*
- ¹⁰⁶*Department of Physical Sciences, Cork Institute of Technology, Bishopstown, Cork, Ireland*
- E-mail:*
Dariusz.Gora@desy.de, Elisa.Bernardini@desy.de, Robert.Franke@desy.de

ABSTRACT: We describe and report the status of a neutrino-triggered program in IceCube that generates real-time alerts for gamma-ray follow-up observations by atmospheric-Cherenkov telescopes (MAGIC and VERITAS). While IceCube is capable of monitoring the whole sky continuously, high-energy gamma-ray telescopes have restricted fields of view and in general are unlikely to be observing a potential neutrino-flaring source at the time such neutrinos are recorded. The use of neutrino-triggered alerts thus aims at increasing the availability of simultaneous multi-messenger data during potential neutrino flaring activity, which can increase the discovery potential and constrain the phenomenological interpretation of the high-energy emission of selected source classes (e.g. blazars). The requirements of a fast and stable online analysis of potential neutrino signals and its operation are presented, along with first results of the program operating between 14 March 2012 and 31 December 2015.

KEYWORDS: Neutrino detectors, Gamma telescopes

Contents

1	Introduction	1
2	Selection of target sources	3
3	The IceCube detector and IACT partners	5
4	Neutrino event selection	5
4.1	Muon Filter	6
4.2	Online Level 2 Filter	7
4.3	NToO selection variables	9
4.4	NToO cut optimization	11
4.5	Properties of the neutrino sample	13
5	The time-clustering algorithm	14
5.1	Alert rate, detection probability	17
6	Data stability monitoring	18
6.1	Rate measurements and data quality assessment	19
6.2	Stability-score calculation	19
6.3	Implementation of the stability-score calculation	21
7	Technical design of the alert system	21
8	Monitoring of alert system	22
9	Results of NToO program	25
10	Recent and upcoming improvements	27
11	Summary and Conclusions	30
12	Appendix	35

1 Introduction

Observations of astrophysical neutrinos may help to answer some of the most fundamental questions in astrophysics, in particular the mystery of the source of cosmic rays (for a general discussion see [1]). For neutrinos in the TeV range, prime source candidates are Galactic supernova remnants [2]. Neutrinos in the PeV range and above are suspected to be produced by active galactic nuclei (AGN) and gamma ray bursts (GRB) with many AGN models predicting a significant neutrino

flux [3–5]. However, the recent results from the IceCube Collaboration strongly disfavor GRBs as sources of the highest energy cosmic rays [6]. Recently, the IceCube Collaboration has also reported the first observation of a cosmic diffuse neutrino flux which lies in the 100 TeV to PeV range [7]. Individual neutrino sources, however, could not be identified up to now. While many astrophysical sources of origin have been suggested [8], there is not yet enough information to narrow down the possibilities to any particular source or source class.

Gamma-ray observations by imaging atmospheric-Cherenkov telescopes (IACTs) such as VERITAS [9], HESS [10] or MAGIC [11] have also a potential to find hadronic γ -rays from the neutrino directions and to identify neutrino sources [12, 13]. The expected neutrino flux from observed high-energy gamma-ray fluxes of blazars in their brightest states (e.g. the flares of Markarian 501 in 1997 [17] and 2005 [18], Markarian 421 in 2000/2001 [19] and 2008 [20] and PKS 2155-304 in 2006 [21]) can be at the level of the neutrino flux detected by the high-energy neutrino telescopes [14–16].

For sources which manifest large time variations in the emitted electromagnetic radiation, the signal-to-noise ratio can be increased by searching for periods of enhanced neutrino emission (a time-dependent search). Of special interest is the relation of these periods of enhanced neutrino emission with periods of strong high-energy gamma-ray emission. However, IACTs have a duty cycle limited to the clear, dark nights (roughly 10% of total time), such correlation studies are not always possible after the neutrino flare has occurred. Therefore, it is desirable to ensure the availability of simultaneous neutrino and high-energy gamma-ray data for periods of interest. This can be achieved by an online neutrino flare search that alerts the partner IACT experiments when an elevated rate of neutrino events from the direction of a source candidate is detected. Such a Neutrino Triggered Target of Opportunity program (NToO), using a list of pre-defined sources, has been developed and has been operating since 2006 using the AMANDA neutrino telescope to initiate gamma-ray follow-up observations by MAGIC [24, 25].

Similarly, one can conduct a search for neutrinos from short transient sources (with a time scale of 100 seconds), such as gamma-ray bursts (GRBs) (see e.g. [27]) and core-collapse supernovae (SNe) (see e.g. [28]). These sources are most accessible in X-ray and optical wavelengths, where one can observe the GRB afterglow or the rising SN light curve, respectively. Similarly to IACTs, the field of view and observation time of X-ray and optical telescopes are limited. Since identification of a GRB or SN is only possible within a certain time range (a few hours after a GRB and a few weeks after a SN explosion), it is important to obtain electromagnetic data within these time frames. To accomplish this, a NToO program triggering optical and X-ray follow-up of short neutrino transients has been operating since 2008 [29, 30]. Upon observing multiplets of neutrino candidates (at least two within 100 seconds and within 3.5° (angular resolution), from any direction) alerts are sent to the Robotic Optical Transient Search Experiment (ROTSE) [31]¹ and the Palomar Transient Factory (PTF) [32] for optical observations, and to Swift [33, 34] for X-ray follow-up, depending on the multiplet’s significance.

We present here a refined and enhanced implementation of the NToO system using the IceCube Neutrino Observatory (see also [26]). An important goal of this program was to establish and to test procedures to trigger promptly the gamma-ray community to collect high-sensitive VHE data

¹ROTSE was used from 2008-2014 and it is not operational anymore.

from specific sources during periods of time when IceCube measures a potential increase in their neutrino flux. The program is based on a multi-step neutrino selection that is applied online at the South Pole. An alert is sent to the partner telescopes MAGIC and VERITAS in the case that a statistically significant cluster of neutrinos is observed from any of the monitored sources. If the source were to be found in an enhanced flux state by the IACT follow-up observation, the combination of the neutrino observation and the very high-energy gamma-observation could help to establish the discovery of neutrino point sources. Furthermore, combining the two observations would increase the potential insight into the physical processes in the source that lead to the flare.

The structure of the paper is the following: Section 2 defines the sources used in the NToO system. Section 3 focuses on the short description of the IceCube and IACTs detectors and their detection principle. In Section 4 the NToO neutrino event selections and the properties of the final neutrino sample are shown. Section 5 describes how the significances of neutrino clusters in the NToO are calculated. Sections 6, 7, 8 describe the technical design and implementation of the NToO system. In Section 9 we present first results of the program operating between 14 March 2012 and 31 December 2015. In Section 10 recent and upcoming improvements of the NToO system are discussed. Finally, in Section 11 a short summary is given.

2 Selection of target sources

The probability of discovering extraterrestrial neutrino point sources varies with the phenomenology of the accelerators and of their emission mechanisms. Coincident observation of gamma rays and neutrinos might be possible for sources where charged and neutral mesons are produced simultaneously from hadronic p-p or p- γ interactions. These hadronic processes may be present in variable extragalactic objects such as BL Lacs or flat-spectrum radio quasars (FSRQs), as well as in Galactic systems like microquasars and magnetars.

Blazars, a subset of radio-loud active galactic nuclei with relativistic jets pointing towards the Earth [41] are commonly classified based on the properties of the spectral energy distribution (SED) of their electromagnetic emission. The blazar SED features two distinctive peaks: a low-energy peak between IR and X-ray energies, attributed to synchrotron emission of energetic electrons, and a high-energy peak at gamma-ray energies, which can be explained by several and possibly competing interaction and radiation processes of high-energy electrons and high-energy nuclei [42]. It has been suggested that blazar SED follow a sequence [43–45] in which the peak energy of the synchrotron emission spectrum decreases with increasing blazar luminosity. Accordingly, blazars can be classified into low synchrotron peak (LSP), intermediate synchrotron peak (ISP) and high synchrotron peak (HSP) objects, a classification scheme introduced in [46]. A second classifier is based on the prominence of emission lines in the SED over the non-thermal continuum emission of the jet. FSRQs show Doppler-broadened optical emission lines [47], while in the BL Lac objects the emission lines do not exist, or are hidden in a strong continuum emission.

The probability for detection of an individual AGN neutrino flare can be estimated based on the predictions of different mechanisms for the observed electromagnetic emission at high energies [3, 4]. A common feature of several models is that the class of high-energy peaked HSP is expected to have lower gamma luminosity as compared to low-energy peaked LSP and FSRQs, if the observed high-energy gamma-ray emission is largely the result of interactions of protons with ambient or

self-produced radiation. With high target matter density, the neutrino yield can be highest when the very high-energy gamma-ray emission is strongly attenuated by internal absorption (although the cutoff energy is somewhat uncertain). In the case of pp-dominated scenarios, the conclusions are different [4], favoring LSP to FSRQs. In all cases, the availability of simultaneous information on high-energy gamma-ray emission and neutrinos is crucial for distinguishing between different production models.

The most interesting targets for gamma-ray follow-up observations triggered by IceCube alerts are promising sources of TeV neutrinos, which are either known to exhibit a bright GeV flux in gamma rays and show extrapolated fluxes detectable by IACTs, or are already detected by IACTs and are variable. We consider two different target source lists. One list was selected based on the the second *Fermi*-LAT point-source catalog [36]². The following criteria were applied:

- Redshift < 0.6 ³
- *Fermi*-LAT variability index > 41.64 (corresponding to the 99% confidence level of the source being variable, see [36] for the definition of this quantity)
- Power-law spectral index as observed with *Fermi*-LAT < 2.3 (BL Lacs only⁴)
- *Fermi*-LAT flux $[1 - 100\text{GeV}] > 1 \cdot 10^{-9} \text{ph cm}^{-2} \text{s}^{-1}$ (BL Lacs only)
- *Fermi*-LAT flux $[0.1 - 1\text{GeV}] > 7 \cdot 10^{-8} \text{ph cm}^{-2} \text{s}^{-1}$ (FSRQs only⁵)

These selection criteria result in 21 sources on the list in total (three FSRQs and 18 BL Lacs). This list of target sources was combined with lists provided by the partner experiments (currently MAGIC and VERITAS) covering the Northern Hemisphere (declination $\delta > 0^\circ$). All known potentially variable VHE sources and all sources in the *Fermi*-LAT monitored-sources list [39] with declination larger than 0° are used. In total 109 sources are included in the follow-up program for the 2012/2013 IceCube season, see Table 6 in Appendix. As we can see from this table 43/(31) sources are present only in the VERITAS/(MAGIC) list and 35 sources are in the list for both experiments. From November 2013 to December 2015, the number of sources were reduced⁶ to 83 i.e. 5 for MAGIC; 65 for VERITAS, and 13 sources are present in both lists, see Table 7 in Appendix. In principle, the neutrinos could also come from unknown sources anywhere in the sky. However, such an all-sky search was not feasible at the time the program was started due to limiting computing resources at the South Pole. Furthermore, an all-sky search suffers from large trial factors compared to the pre-defined source list search.

²The third *Fermi*-LAT point-source catalog [37] or catalog of hard *Fermi*-LAT sources [38] would have been more suitable, but it was not available when the selection criteria were established and the program started.

³The MAGIC and VERITAS telescopes have recently detected sources with $z \sim 0.94$, PKS 1441+25 [40, 48] and B0218+357 [49]); therefore this selection criterion ("cut") will be extended to $z = 1$ for the next IceCube observing season 2016/2017.

⁴As shown in [4] for pp-scenario only BL Lacs with the spectral index below 2.2 - 2.3 are promising candidates for IceCube detection, see Figure 2 in this paper.

⁵As shown in [3] for p - γ -scenario only FSRQs can be effective for interpretation of gamma-ray fluxes up to GeV energies.

⁶For MAGIC, the number of sources was reduced in order to fit to amount of observation time that was granted by MAGIC time allocation committee.

3 The IceCube detector and IACT partners

The IceCube Neutrino Observatory [54–56] is located at the geographic South Pole and was completed at the end of 2010. The goal of the detector is to serve as a neutrino telescope, allowing observations of neutrinos of astrophysical origin in the TeV and PeV energy range. Cherenkov light produced by the secondary leptons from neutrino interactions in the vicinity of the detector is used to detect these neutrinos. IceCube is also sensitive to downward-going high-energy muons and to neutrinos produced in cosmic-ray-induced air showers. These events represent a background for most IceCube analyses.

For the studies presented here, only events produced by charged-current interactions of muon neutrinos are considered, because of the long range of the secondary muons which allows for reconstructing the arrival direction of these events with good accuracy. The pointing information relies on the secondary muon direction, which at energies above a TeV differs from the original neutrino direction by less than the angular resolution of the detector.

The program presented in this work sends alerts to IACTs for follow-up observations. IACTs detect photon-induced air showers by means of the Cherenkov light from the highly relativistic charged particles in the shower. Due to the interplay between the emission geometry and the altitude dependent index of refraction, the Cherenkov light flash (~ 10 ns duration) is mainly concentrated in a light pool with a radius of ~ 120 m (for gamma or electron showers) on the ground. A telescope located inside the light pool can reflect the light into a PMT camera. Cherenkov images of the showers are used to differentiate between gamma-ray signal and background, and to reconstruct the energy and the incoming direction of the gamma rays.

The MAGIC telescope array is located on the Roque de los Muchachos Observatory (28.8° N, 17.9° W; 2200 m above sea level), at the Canary Island of La Palma (Spain). The MAGIC array consists of two telescopes, placed 85 m apart, each with a primary mirror of 17 m diameter. The MAGIC telescopes, with a field of view of 3.5° , are able to detect cosmic gamma rays in the range 50 GeV–50 TeV. The latest performance of MAGIC is reported in [22].

VERITAS is an array of four 12-m diameter imaging atmospheric-Cherenkov telescopes located at the Fred Lawrence Whipple Observatory in southern Arizona ($31^\circ 40' \text{N}$, $110^\circ 57' \text{W}$) at an altitude of 1.3 km. Each of the individual telescopes have a 3.5° field of view. Full details of the VERITAS instrument performance and sensitivity are given in [23].

4 Neutrino event selection

This section describes the online neutrino selection that is the basis for the NToO system. As the computing resources at the South Pole are limited, different types of software triggers are applied to lower the data event rate. The most important for the purposes of this work is the *Simple Multiplicity Trigger* (SMT8) which requires eight triggered optical modules (i.e. four coincidence pairs) anywhere in the detector within $5 \mu\text{s}$. Most of the events which are selected by this trigger are composed of muons produced by cosmic rays in the atmosphere above the detector (about 2.5 kHz at trigger level in the 86-string configuration). As the data volume produced at trigger level is still too large to be transferred via satellite, a first selection has to be applied directly at the South

IceCube data taking period	Start	End
IC-2011	2011 May 13	2012 May 16
IC-2012	2012 May 16	2013 May 3
IC-2013	2013 May 3	2014 May 5
IC-2014	2014 May 5	2015 May 18
IC-2015	2015 May 18	2016 May 20

Table 1. Summary of IceCube data taking periods (seasons) used by NToO searches

Pole by using the so-called *Muon Filter*. This filter aims to select well-reconstructed muon tracks of any direction, i.e. from the full sky.

The event selection takes place in several steps, called “levels“ in IceCube. The *Muon Filter* constitutes the first filtering level. It is a standard IceCube filter and not specific to the program presented here. The subsequent *Online Level 2 Filter* is based on the input from the *Muon Filter* and was specifically developed to enable online analyses. Currently the *Online Level 2 Filter* forms the basis of the optical and X-ray follow-up program and the NToO system presented in this work. Based on cut variables calculated from the *Online Level 2 Filter*, an online neutrino event selection was implemented. The main goal is to achieve a high efficiency for valid neutrino events with the highest possible rejection of background.

4.1 Muon Filter

The *Muon Filter* event-selection algorithm is the basis for many standard IceCube muon-neutrino analyses, e.g. the searches for neutrino point sources, searches for neutrinos from gamma-ray bursts and measurements of the atmospheric muon-neutrino flux. The input to the *Muon Filter* is all of the events that trigger the SMT8. All events triggering the SMT8 are reconstructed with the *Linefit* first-guess algorithm as described in [57]. The result from this track fit forms the input to a single-photoelectron (SPE) likelihood fit [51, 57], which uses only the time and charge of the first hit on each DOM. The *Muon Filter* decision is based on variables calculated from the SPE fit.

The track reconstructions and cuts applied in the *Muon Filter* have been stable over several years. However, improvements to reconstruction algorithms, changes in the available satellite transfer bandwidth, or changes in the data serialization format lead to small adjustments from season to season. The IceCube seasons important for this work are listed in the Table 1. For example, in the IC-2012 season an improved *Linefit* algorithm was used, which uses a linear fit with reduced weights for outliers [58].

The *Muon Filter* divides the sky into two regions in which different selection techniques are applied to remove background events. In the first region (defined by the zenith angle $\theta \geq 78.5^\circ$) the background events are down-going muons mis-reconstructed as up-going (or slightly above the horizon), which in fact originate from cosmic-ray-induced air showers. The main discriminants to remove these events are parameters characterizing the reconstruction quality of the event. In the second region (zenith angle $\theta < 78.5^\circ$) both signal and background events have the same signature, namely high-energy muon tracks. As the energy spectrum of muons in cosmic-ray air showers ($\Phi(E) \sim E^{-3.7}$) is much steeper than the expected signal spectra, cuts on energy-related variables are an efficient way to reduce this background. However, as the current NToO is only implemented

for zenith angles $\theta > 90^\circ$ the event-selection cuts in the second region will not be described in detail.

In the first region the *Muon Filter* uses a cut variable derived from the value of the likelihood of the SPE track fit. The definition of the cut variable is similar to the scaled log-likelihood of the fit. All events which are reconstructed with a zenith angle $\theta_{\text{SPE}} \geq 78.5^\circ$ and that fulfill

$$-\log_{10}(\max \mathcal{L}_{\text{SPE}})/(N_{\text{DOM}} - 3) \leq 8.7, \quad (4.1)$$

where $\max \mathcal{L}_{\text{SPE}}$ is the maximum value of the likelihood function of the SPE track fit and N_{DOM} denotes the number of triggered DOMs in that event, passed the filter. The efficiency of the *Muon Filter* for atmospheric neutrinos is about 87% with respect to SMT8. Neutrinos following a spectrum of the form $\Phi(E) \sim E^{-2}$ are selected with an efficiency of approximately 93% with respect to SMT8. The cuts remained unchanged between the different IceCube seasons i.e. from IC-2011 to IC-2014. The total event passing rate of the *Muon Filter* amounts to approximately 45 Hz, out of which about 18 Hz consists of events reconstructed with zenith angle $\theta_{\text{SPE}} > 90^\circ$.

4.2 Online Level 2 Filter

While the *Muon Filter* provides a sample of candidate neutrino events it is still heavily background-dominated (compared to the atmospheric-neutrino rate of about 10 mHz at the trigger level). In order to apply further cuts with a high signal efficiency, more elaborate reconstructions with an improved angular resolution are needed. As an example, the multi-photoelectron (MPE) likelihood function, which uses the temporal and amplitude information of the PMT pulses, is applied after several iterations of SPE likelihood fit. The MPE algorithm includes a probability distribution function (PDF) that describes the scattering of photons in the ice, and is fully described in [57]. Further reconstructions that estimate the angular reconstruction uncertainty are also helpful for subsequent analyses. This combination of additional reconstruction and event-selection cuts is referred to as the *Online Level 2 Filter*.

The SPE fit used as an input to the *Muon Filter* has limited angular resolution compared to an MPE fit. During the first season of running the IceCube in its full 86-string configuration (IC-2011), the limited CPU resources at the South Pole prohibited applying more resource-intensive reconstructions to all events that passed the *Muon Filter*. Therefore, it was necessary to apply event-selection cuts to the events passing the *Muon Filter* before additional reconstruction could be performed. The computing resources at the South Pole were expanded prior to the second full season of IceCube in its 86-string configuration (IC-2012). This expansion made it possible to run some reconstruction (a double-iteration SPE fit and the MPE fit) before applying the *Online Level 2* cuts.

In the up-going region, the main criteria to distinguish the mis-reconstructed atmospheric-muon background from the neutrino events are quality parameters of the reconstructed track. Several variables derived from the single-iteration SPE fit were used to identify these well-reconstructed tracks and to suppress mis-reconstructed air-shower muons during the IC-2011 season. During the IC-2012 season these variables were derived from the MPE fit. The most important variables are:

The Scaled Log-Likelihood In a maximum-likelihood fit the value of the likelihood at the maximum divided by the number of degrees of freedom of the fit can measure the fit quality. The scaled

likelihood of the track fit is

$$S_{\text{LogL}}(x) = \frac{-\log_{10}(\max \mathcal{L})}{N_{\text{DOM}} - x}, \quad (4.2)$$

where N_{DOM} is the number of hit DOMs, and x the numbers of parameters determined by the fit, usually five: two angles, and three coordinates. However, it has been shown empirically that $S_{\text{LogL}}(5)$ is energy-dependent for the track fits employed in IceCube. Thus, a cut on $S_{\text{LogL}}(5)$ variable introduces a bias against well-reconstructed low-energy events. In order to reduce this energy dependence bias, the different values of x is used i.e. $x = 3.5$ for NToO and $x = 4.5$ for optical and X-ray follow up. This variable is especially useful for identifying mis-reconstructed muon tracks.

Number of Direct Hits (N_{Dir}) Another measure of the track quality is the number of DOMs that have registered a hit with a very small time residual $t_{\text{res}} \in [-15 \text{ ns}, 75 \text{ ns}]$ with respect to the arrival time expected for Cherenkov emission from the reconstructed muon track. Such hits are called ‘‘direct hits’’. The number of direct hits N_{Dir} is calculated using only the first registered photon in each DOM. A photon causing a direct hit has undergone less scattering in the ice and thus can contribute more information to the directional reconstruction. The number of direct hits is therefore related to the quality of the track reconstruction.

Direct Length (L_{Dir}) The distance between the projected direct hits onto the reconstructed track is referred to as the ‘‘direct length’’, L_{Dir} . The hits defining the direct length result from the least-scattered photons and hence contribute the most to the reconstruction. If L_{Dir} is large, the lever arm for the reconstruction is longer, generally resulting in smaller reconstruction errors. Therefore, selecting events with larger L_{Dir} selects the events most valuable for a point-source analysis.

The cut variables described above have been combined to achieve good background rejection as well as reasonable signal efficiency. Events that are reconstructed as up-going (zenith angle $\theta_{\text{SPE}} > 82^\circ$) and fulfill

$$S_{\text{LogL}}(4.5) \leq 8.3 \text{ or } \log_{10}\left(\frac{Q_{\text{Tot}}}{p.e.}\right) \geq 2.7$$

$$\text{or } \left(\frac{L_{\text{Dir}}[m]}{160}\right)^2 + \left(\frac{N_{\text{Dir}}}{9}\right)^2 \geq 1 \quad (4.3)$$

where Q_{Tot} is the total charge of the event in photoelectrons (p.e.), are selected by the *Online Level 2 Filter*. The pre-selection criterion based on the number of direct hits (N_{Dir}) and the direct length (L_{Dir}) in Eq. (4.3) is called the ‘‘direct ellipse’’ cut. The background atmospheric-muon events tend to have short direct lengths and a small number of direct hits since, if they are mis-reconstructed as upward-going muon tracks, the hit pattern tends to match poorly. The direct ellipse cut keeps $\sim 74\%$ of atmospheric neutrinos and $\sim 76\%$ of astrophysical neutrinos while rejecting $\sim 93\%$ of atmospheric muons.

Quality parameters of the track reconstruction A critical parameter in a maximum-likelihood-based search for neutrino point sources is the error of the reconstruction for each event. As this can only be determined on an event-by-event basis with simulated data, an estimate has to be used for experimental data. Two different approaches are applied in IceCube: the *Paraboloid fit*

and the *Cramér-Rao Resolution Estimate*. The *Paraboloid fit* scans the likelihood space around the minimum determined in the track fit by varying the fit parameters. The resulting points in likelihood space are fitted with a parabola [52]. Due to the repeated evaluation of the likelihood function this method can be too slow to be used in the online filtering, especially for high-energy events with a large number of hit DOMs. The *Cramér-Rao Resolution Estimate* is the uncertainty on the reconstructed track direction given by the log-likelihood-based track reconstruction estimated by a method based on the Cramér-Rao inequality [53]. As the calculation involves no minimization of a likelihood it is considerably faster (and have a similar performance) than the *Paraboloid fit* and thus is the preferred method to be used in online analysis, also in NToO. Since the likelihood used in the track fit fully describes the Cherenkov light emission and propagation, both angular uncertainty estimates, the *Paraboloid fit* and the Cramér-Rao method, show an energy-dependent bias in the ratios of the estimated to the true angular uncertainty. This bias can be calibrated using Monte Carlo events to derive a correction factor which is a function of the reconstructed event energy.

The event rate after application of the *Online Level 2 Filter* is reduced to approximately 2 Hz (in the up-going region). More than 99% of well-reconstructed signal neutrinos (i.e. reconstructed within 3° from their true direction) from an E^{-2} energy spectrum are retained, with respect to the number which pass the *Muon Filter*.

In subsequent analysis steps, more-computationally-intensive reconstructions can be performed, including angular-resolution estimators, energy estimators and likelihood fits applied to different subsets of the recorded photons.

4.3 NToO selection variables

The background rejection of the *Online Level 2 Filter* is still not sufficient for NToO data analyses, since the sample is still dominated by mis-reconstructed atmospheric muons. Only approximately 1 out of every 1000 events is a neutrino. Thus, based on variables from the *Online Level 2 Filter* reconstructions the final event sample is selected by employing additional quality cuts. The following additional cut variables are used:

Split Fits The track reconstruction for a correctly-reconstructed up-going track should be stable against changes to the set of DOMs used for reconstruction. On the other hand, for two co-incident down-going muons wrongly reconstructed as one up-going track, or for other cases of mis-reconstruction, changes to the DOM set will have a much larger impact on the reconstructed direction. This is the rationale for splitting the DOM set used in the reconstruction into two parts and subsequently performing a maximum-likelihood fit on each part separately. Different criteria can be used to split the DOM set:

- geometrical splitting divides the hits according to their position with respect to the center of gravity (COG) of all hits. The center of gravity is calculated as

$$\vec{x}_{\text{COG}} = \frac{\sum_{i=1}^{N_{\text{DOM}}} q_i \times \vec{x}_i}{\sum_{i=1}^{N_{\text{DOM}}} q_i} \quad (4.4)$$

where \vec{x}_i are the positions of the individual hit DOMs and q_i the charge of each hit DOM. The center of gravity \vec{x}_{COG} is then projected onto the track obtained with the MPE fit, yielding the

point $\vec{x}_{\text{COG}}^{\text{proj}}$. Each hit location is then also projected onto the track, and compared to $\vec{x}_{\text{COG}}^{\text{proj}}$. Hits whose projections lie on one side of $\vec{x}_{\text{COG}}^{\text{proj}}$ are sorted into one set, hits whose projections lie on the other side are sorted into a second set.

- time-based splitting divides the hits into two sets by comparing each hit to the mean of all hit times t_{mean} . Hits that fulfill $t_i \leq t_{\text{mean}}$ are sorted into one set, hits that fulfill $t_i > t_{\text{mean}}$ are sorted into another set.

For each of the four subsets of hits a standard *Linefit* is performed which acts as a seed for a two-iteration SPE maximum-likelihood fit. The zenith angle θ_i resulting from the SPE fit, when only the time and charge of the first hit on each DOM are taken into account in the reconstruction, is used to define the cut variable

$$\Delta_{\text{Split/SPE}} = \max_{i \in \text{split fits}} (\cos \theta_i - \cos \theta_{\text{SPE}}). \quad (4.5)$$

Bayesian Likelihood Ratio The probability that an event selected by the *Online Level 2 Filter* and reconstructed as up-going (i.e. zenith angle $\theta_{\text{SPE}} > 90^\circ$) is truly a neutrino-induced muon and not a mis-reconstructed air-shower muon is very small ($\sim 10^{-3}$). A useful additional cut variable can be derived by forcing a down-going track fit and calculating the likelihood ratio to the SPE fit. This cut is motivated by a Bayesian approach [61] to event reconstruction. Bayes' Theorem in probability theory states that for two assertions A and B ,

$$P(A|B)P(B) = P(B|A)P(A),$$

where $P(A|B)$ is the probability of assertion A given that B is true. Identifying A with a particular muon track hypothesis μ , and B with the data recorded for an event in the detector, we have

$$P(\mu|\text{data}) = \mathcal{L}_{\text{SPE}}(\text{data}|\mu)P(\mu),$$

where we have dropped a normalization factor $P(\text{data})$, which is a constant for the observed event. The function \mathcal{L}_{SPE} is the regular SPE likelihood function, and $P(\mu)$ is the so-called prior function, which is the probability of a muon passing through the IceCube detector, and is given by

$$P(\mu) = 2.50 \cdot 10^{-7} \cos \theta^{1.68} \cdot \exp\left(-\frac{0.78}{\cos \theta}\right), \quad (4.6)$$

This function is a fit to the simulated zenith-angle distributions of down-going cosmic ray muons triggered by IceCube, see also [62, 63] for more details. By accounting in the reconstruction for the fact that the flux of down-going muons from cosmic-rays is many orders of magnitude larger than that of up-going neutrino-induced muons, the number of down-going muons that are mis-reconstructed as up-going is greatly reduced.

The difference of the logarithms of the SPE likelihood fit and the Bayesian-fit likelihood

$$\Delta_{\text{SPE/Bayesian}} = \log_{10} \mathcal{L}_{\text{SPE}} - \log_{10}(\mathcal{L}_{\text{SPE}}(\text{data}|\mu)P(\mu)) \quad (4.7)$$

is another useful cut variable, especially for events that have been reconstructed with a zenith angle close to the horizon.

4.4 NToO cut optimization

For neutrino searches, muons produced in cosmic-ray-induced air showers are the dominant background in IceCube for tracks coming from the Southern Hemisphere. They trigger the detector with a rate 10^6 times higher than atmospheric neutrinos. Tracks from the Northern Hemisphere originate mostly from atmospheric neutrino interactions that produce muons. BOTH of these background components are simulated using Monte Carlo studies.

Cosmic-ray air showers are simulated using a patched version of CORSIKA [64]. The spectra of cosmic-ray primaries are sampled from the phenomenological *Polygonato* model [65] and the background datasets were produced with the Sybill [66] hadronic-interaction model. A sizable fraction of events in the IceCube detector include several muons from distinct air showers. These so-called coincident air-shower events are simulated as well.

Neutrino events are simulated based on the Monte Carlo generator ANIS [67]. ANIS generates neutrinos, propagates them through the Earth and finally forces them to interact in a volume around the detector. As different primary neutrino spectra are needed by different analyses, one usually simulates a generic primary spectrum $dN/dE_\mu \sim E_\nu^{-\gamma}$ where $\gamma = 1$ or $\gamma = 2$. The events can be re-weighted to the desired spectrum for each analysis. The output of the neutrino generator in the case of a charged-current ν_μ interaction is a muon produced at the interaction vertex and the accompanying hadronic cascade. The cascade is not simulated in detail.

The simulation of the muon propagation and the muon energy loss is essential to obtain the light distribution in the detector. A software package called PROPOSAL [68] is employed for that purpose. PROPOSAL calculates the continuous energy loss of the muon as well as the stochastic losses due to bremsstrahlung, pair production, photonuclear interactions and delta electrons. Finally, the detector simulation is concerned with the response of the PMTs to detected photons, the digitization of the PMT waveform in the DOM, and the trigger system. This is done by the IceCube software framework called IceTray [69].

In order to achieve the best possible sensitivity, the cuts on the variables described in the previous section have been optimized together in independent zenith-angle regions. For each combination of cut values, the rate of remaining data events was used as the approximation for the background rate. The rate of signal events for a given flux was estimated from neutrino simulations, assuming a neutrino flux with a spectral index $\gamma = 2$. This is motivated by the fact that diffuse shock acceleration leads to power-law spectra with a spectral index around 2 [72, 73] and neutrinos originating in cosmic rays interactions near the source are expected to follow a similar spectrum.

The cut optimization was repeated for flares of different durations ranging from 1 day to 20 days; as an example see Figure 1. As traditional minimizers like MINUIT [59] were found to converge on local minima a particle swarm optimization algorithm was used [60]. For simplicity the minimization assumes that the flare time window is known.

In the binned point-source method the radius of the on-source bin is a free parameter. The optimal bin size as a function of zenith depends on the angular resolution and the background rate of atmospheric neutrinos at each zenith angle. The search-bin radius has also been optimized together with the cut variables to yield the best sensitivity.

The first set of the NToO cuts was optimized using the IC-2011 season, and later redefined

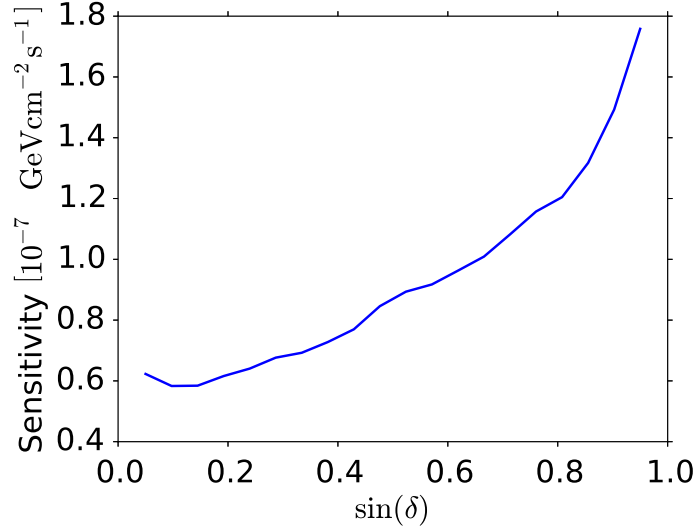


Figure 1. Simulated IceCube sensitivity as a function of source declination to a neutrino flux with $dN/dE \sim E^{-2}$ for a neutrino flare length of 10 days and for the IC-2012 data set. The sensitivity did not change significantly for other IceCube data seasons. The sensitivity is defined as the flux required for a 3 sigma detection with a probability of 90%.

using data from the IC-2012 season. Only the cut on the Bayesian likelihood ratio was changed.

Cut Level	Selection criterion	Atms. μ (mHz)	Data (mHz)	Atms. ν_μ (mHz)	Astro. $\times 10^{-3}$ (mHz)
0	$\cos \theta_{\text{MPE}} \leq 0$	1010.5	1523.81	7.166	6.23
1	$S\text{LogL}(3.5) \leq 8$	282.49	504.44	5.826	5.62
2	$N_{\text{Dir}} \geq 9$	8.839	22.01	3.076	4.06
3	$((\cos \theta_{\text{MPE}} > -0.2) \text{ AND } (L_{\text{Dir}} \geq 300 \text{ m}))$ OR $((\cos \theta_{\text{MPE}} \leq -0.2) \text{ AND } (L_{\text{Dir}} \geq 200 \text{ m}))$	1.124	4.30	2.313	3.69
4	$\Delta_{\text{Split/MPE}} < 0.5$	0.100	2.15	1.899	3.26
5	$((\cos \theta_{\text{MPE}} \leq -0.07))$ OR $((\cos \theta_{\text{MPE}} > -0.07) \text{ AND } (\Delta_{\text{SPE/Bayesian}} \geq 35))$	0.080	2.08	1.880	3.25
6	$((\cos \theta_{\text{MPE}} \leq -0.04))$ OR $((\cos \theta_{\text{MPE}} > -0.04) \text{ AND } (\Delta_{\text{SPE/Bayesian}} \geq 40))$	0.075	2.06	1.875	3.24

Table 2. IceCube neutrino selection cuts and corresponding passing event rate for the IC-2012 season. At an final selection an event has to fulfill all cut criteria to pass the selection (i.e. a logical AND condition between the cut levels is applied). The atmospheric-neutrino flux is based on the prediction by Honda [71], but atmospheric-muon rate is calculated from CORSIKA simulations. The event rate for IceCube data stream corresponds to the total livetime of 332.36 days. The astrophysical neutrino flux is estimated assuming $dN/dE = 1 \cdot 10^{-8} \text{ GeVcm}^{-2}\text{s}^{-1}(\frac{E}{\text{GeV}})^{-2}$. (Atms. = atmospheric, Astro. = astrophysical)

The final set of smooth cuts resulting from the cut optimization is listed in Table 2 and the

optimal search-bin radius as a function of declination angle ($\delta > 0^\circ$) has been parametrized as

$$r = 1.2^\circ + 1.4^\circ \cdot \sin(\delta). \quad (4.8)$$

Table 2 shows also the influence of each selection cut on event rate for data, simulated atmospheric neutrinos and muons.

The experimental data sample, after application of the *Online Level 2 Filter* (Cut Level 0), consists of 4.3×10^7 events acquired within a total livetime of 332.36 days. At this level, see Table 2, atmospheric muons dominant the contribution to the measured data sample. However, these mis-reconstructed events being truly down-going and reconstructed as up-going are almost removed by our selection criterion, i.e. the passing rate is reduced by 99.9925 % with respect to Cut Level 0. We also see that at the final selection cut the data rate reach the level of atmospheric muon neutrinos, i.e. about 2 mHz, and selection criterion keeps about 52% of the signal events (with respect to Cut Level 0) for an E^{-2} signal neutrino spectrum of astrophysical neutrinos.

The same set of cuts was used for the next IceCube seasons: IC-2013 and IC-2014 thanks the very stable behavior of the IceCube detector and its performance.

4.5 Properties of the neutrino sample

The event selection results in an event rate of about 2 mHz and a median angular resolution of 0.5° for an E^{-2} signal neutrino spectrum. Figure 2 depicts the median angular resolution of the final neutrino sample as a function of neutrino energy and as a function of neutrino declination angle ⁷.

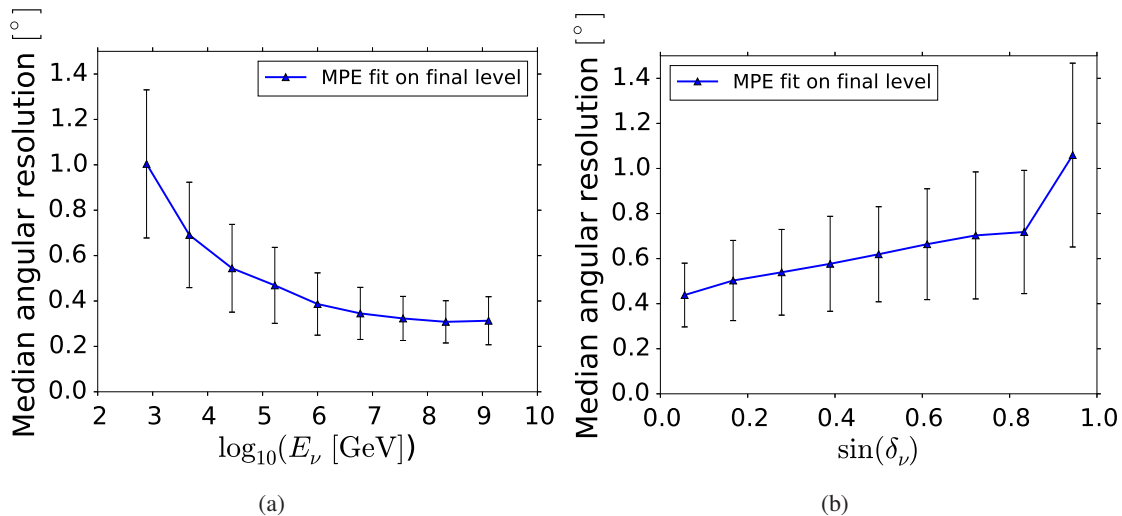


Figure 2. IceCube median angular resolutions based on *Cramér-Rao Resolution Estimator* for the final selected neutrino sample as a function of (true) neutrino energy (left panel) and declination (right panel), assuming in simulation a primary neutrino spectrum with $\Phi(E) \sim E^{-2}$. The error bars depict the 16th and 84th percentile of the angular resolution. Neutrino angular resolution defined as the median of the point-spread function of the true neutrino direction and the reconstructed muon direction.

Figure 3 depicts the effective area for muon neutrinos as a function of neutrino energy in different declination regions. It is worthwhile to note that the effective area reaches only about

⁷IceCube is located at the South Pole, so the relation between zenith angle and declination is given by simply transformation: $\theta = \delta + 90^\circ$.

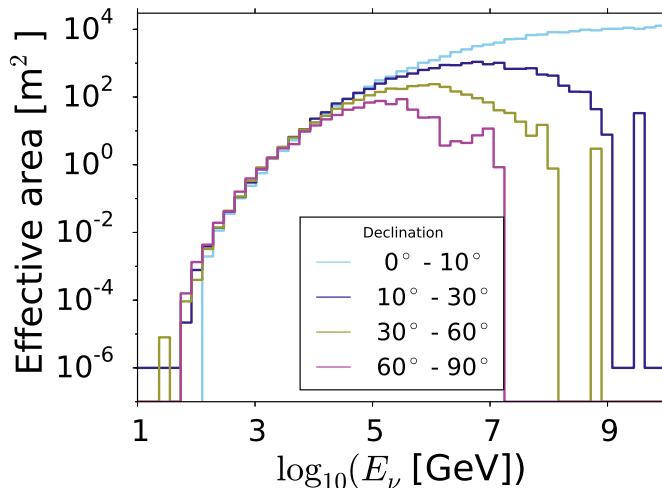


Figure 3. Simulated IceCube effective area as a function of the (true) neutrino energy for the final neutrino selection derived from the 2012/2013 data set. The strongly energy dependent neutrino-nucleon cross section leads to the observed behavior of an effective area that is generally increasing with energy, until neutrino absorption dominates. For larger declinations the effect of neutrino absorption sets in at lower energies due to the longer path through the Earth. The acceptance is similar for other IceCube data seasons.

1 m^2 at $10^{3.2} \text{ GeV}$. For events with declination between 10° and 30° the effective area reaches a maximum of about 1000 m^2 at $10^{6.5} \text{ GeV}$ and begins to drop above $10^{7.5} \text{ GeV}$ due to absorption of neutrinos in the Earth. For neutrinos very close to the horizon ($0^\circ \leq \delta \leq 10^\circ$) and for neutrino energies greater than 10^8 GeV the effective area can reach 10^4 m^2 .

The efficiency of the event-selection cuts with respect to the *Online Level 2 Filter* is depicted in Figure 4 for all events (dashed) and for events that have been reconstructed within angle $\Delta\Psi < 3^\circ$ of their true direction. Well-reconstructed events are selected with an efficiency of more than 60 % above 1 TeV; while the overall peak efficiency of about 80 % is reached between 100 TeV and 10 PeV.

As we already mentioned above, the main selection cuts are optimized for a neutrino power-law spectrum with a spectral index $\gamma = 2$. However, several Galactic gamma-ray sources have energy spectra with energy cutoffs at a few TeV [74], supporting the idea that Galactic neutrino spectra may present cutoff spectra as well [75, 76]. Also, recent IceCube results show that the astrophysical neutrino flux has a neutrino spectrum softer than E^{-2} . The IceCube neutrino flux can be well described by an unbroken power law with best-fit spectral index 2.50 ± 0.09 [70].

Therefore in Table 3 the efficiency of neutrino selection for softer spectral indexes (e.g. 2.5 and 2.7) is also shown. As we can see, for softer spectra, the performance of NToO cuts is about 20 % worse, but the signal efficiency is still above 50% for well-reconstructed events.

5 The time-clustering algorithm

The timescale of a neutrino flare is not fixed *a priori* and thus a simple rolling-time-window approach is not sufficient to detect flares. The time-clustering approach that was developed for an

E^{-2} ($\Delta\Psi_{\text{MPE}} < 3^\circ$)	$E^{-2.5}$ ($\Delta\Psi_{\text{MPE}} < 3^\circ$)	$E^{-2.7}$ ($\Delta\Psi_{\text{MPE}} < 3^\circ$)
52 % (73 %)	43 % (63 %)	39 % (59 %)

Table 3. Efficiency (from simulation) of the neutrino selection cuts with respect to the *Online Level 2 Filter* (in %). The efficiencies for well-reconstructed events (defined as events with $\Delta\Psi_{\text{MPE}} < 3^\circ$) are given in parentheses.

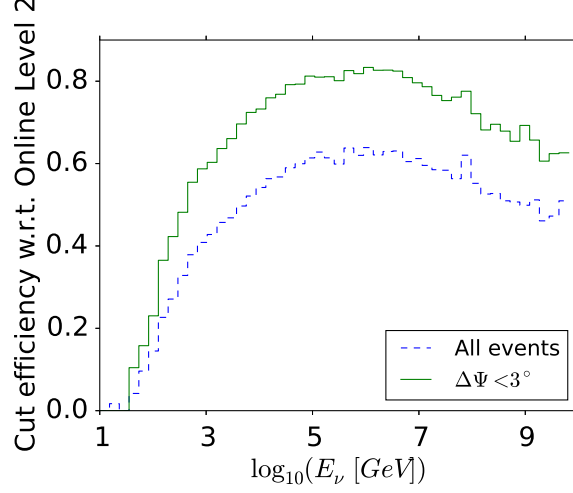


Figure 4. Efficiency of the neutrino-selection cuts for IceCube with respect to *Online Level 2* for all events (blue, dashed line) and events with angular reconstruction error, $\Delta\Psi < 3^\circ$ (green, solid line).

unbiased neutrino flare search [50] looks for any time frame with a significant deviation of the number of detected neutrinos from the expected background. The simplest implementation uses a spatially binned approach where neutrino candidates within a fixed radius around a source are regarded as possible signal events.

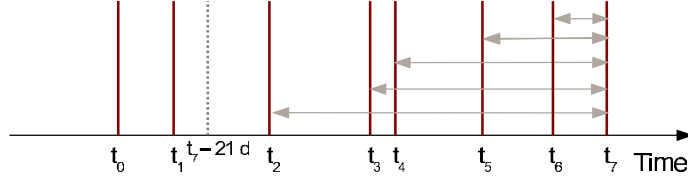


Figure 5. Schematic of the time-clustering algorithm. For an IceCube event in an on-source bin detected at time t_7 the significances of all clusters formed with events detected up to 21 days back are calculated.

If a neutrino event is detected at time t_i from the search bin around a given source, the expected background $N_{\text{bg}}^{i,j}$ is calculated for all other events j within a time window $\Delta t_j = t_j - t_i$ around that bin (see Figure 5). To calculate $N_{\text{bg}}^{i,j}$ the detector efficiency as a function of the azimuth angle and the uptime has to be taken into account. The number of expected background events $N_{\text{bg}}^{i,j}$ in a time window $[t_i, t_j]$ for a source at a certain declination is given by

$$N_{\text{bg}}^{i,j} = t_{\text{up}}^{i,j} \dot{N}(\theta) \epsilon(\Phi(t)) \quad (5.9)$$

where $\dot{N}(\theta)$ is the zenith-angle-dependent rate of data used as background events, $t_{\text{up}}^{i,j}$ uptime in a

time window $[t_i, t_j]$ and $\epsilon(\Phi(t))$ the normalized azimuth distribution of IceCube events (see Figure 6).

The Poisson probability of observing the multiplet (i, j) by chance is then calculated according to

$$p_{\text{obs}} = \sum_{k=N_{\text{obs}}^{i,j}-1}^{\infty} \frac{(N_{\text{bg}}^{i,j})^k}{k!} e^{-N_{\text{bg}}^{i,j}} \quad (5.10)$$

where N_{obs} is the number of detected on-source neutrinos between t_j and t_i . N_{obs} must be reduced by one to take into account the bias introduced by the fact that the background is measured in the time window defined by the j^{th} event. Most very high energy flares detected so far have a duration up to several days, thus we constrain our search for time clusters of neutrinos to 21 days so as to minimize the statistical trial factor penalty.

The probability p_{obs} is often expressed in terms of the distance to the center of a normal distribution measured in units of standard deviations that results in the same cumulative probability in the right tail (e.g. a probability of $\log_{10}(p_{\text{obs}}) = -2.87$ is often quoted as 3σ). If the cluster with the highest significance exceeds a certain threshold (e.g. corresponding to 3σ) the detector stability is first checked and, if appropriate, an alert is sent to a partner experiment (atmospheric-Cherenkov telescope) to initiate a follow-up observation.

The physical layout of the IceCube, with the instrumented strings positioned on a hexagonal grid, results in an increased trigger rate for events that propagate along the symmetry axes. Therefore, the expected number of background events in a time window for a source at a certain right ascension depends on the azimuth-angle range covered during that time. This natural azimuth dependence is reinforced by cut variables that favour events that pass close to many strings (e.g. direct hits and direct length). For time-integrated point-source searches, the azimuth dependence

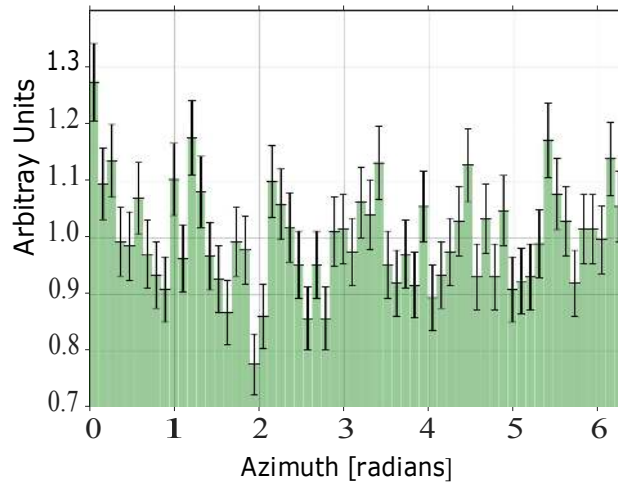


Figure 6. The normalized distribution of IceCube events as a function of azimuth. The dependence is caused by the hexagonal layout of the grid of IceCube strings that produces symmetry axes.

is usually neglected because it is smoothed in right ascension by the rotation of the Earth over

long integration times. However, in a time-dependent analysis the azimuth dependence becomes important for timescales shorter than $t_i - t_j < 2$ days.

The stable uptime between $t_{up}^{i,j}$ in a time window $[t_i, t_j]$ is calculated using the online detector stability monitoring (described in Sec. 6) and combined with information about the start and stop times of the data-taking runs.

5.1 Alert rate, detection probability

Since the NToO aims at the discovery of neutrino flares from astrophysical sources, it is important to define what astrophysical neutrino flux level would trigger an alert.

In Figure 7 (A) we show the flux as a function of declination that results in a trigger probability of 50% for significance thresholds corresponding to 3.0σ and 5.0σ for a flare duration of 10 days, while in Figure 7 (B) the probability of triggering an alert as a function of the neutrino flux, assuming a spectral index $\gamma = 2$ and a flare duration of 10 days, is shown for alert thresholds corresponding to 3σ and 5σ for a source at a declination $\delta = 28.0^\circ$. As we can see from these plots, a signal flux of the form $\Phi(E) = 6 \cdot 10^{-8} \text{ GeVcm}^{-2}\text{s}^{-1} (\frac{E}{\text{GeV}})^{-2}$ will on average trigger an alert with a probability of 50% for an alert threshold of 3.0σ .

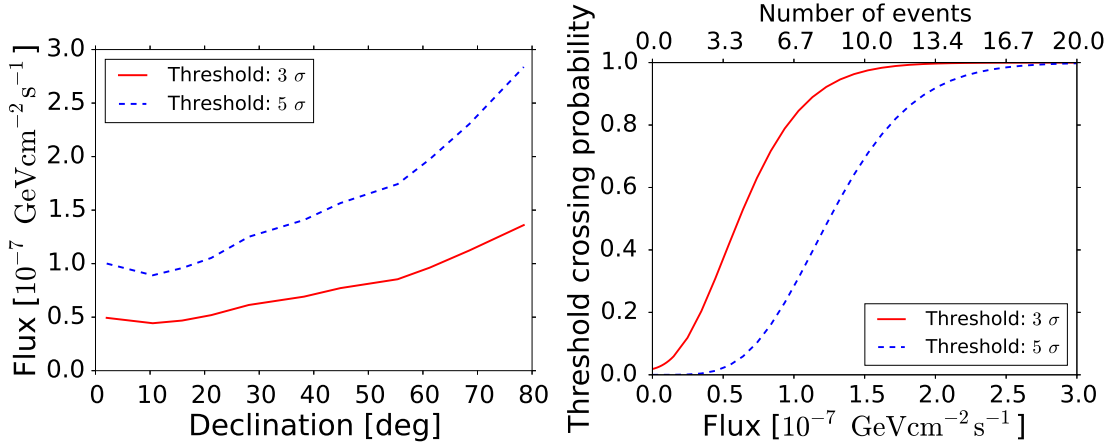


Figure 7. (Left panel) Neutrino flux required by IceCube at a given source declination to trigger an alert with a significance of 3σ (solid line) and 5σ (dashed line) with a probability of 50%. The neutrino spectrum is assumed to be an unbroken power law with a spectral index of 2; the flare duration is 10 days. (Right panel) Probability to trigger an NToO alert as a function of flux for flares with a duration of 10 days at a declination $\delta = 28.0^\circ$, for alert thresholds of 3σ (red, solid line) and 5σ (blue, dashed line). The upper axis shows the number of required events needed for neutrino flux for alert with given significance.

The number of accidental background alerts also needs to be estimated in order to calculate the total significance of all the alerts generated by the program, as well as to set sensible alert thresholds such that the partner observatory is not overwhelmed by follow-up requests. The number of follow-up requests allowed in a given time period is fixed by the Time Allocation Committees of the partner experiments. Figure 8 shows the number of accidental background alerts as a function of the alert significance threshold. For a threshold of 3.2σ (MAGIC) this would result in a fake alert rate of about 0.1 alerts/(source \cdot year). Thus, given the number of sources (around 70) in this

program for the MAGIC experiment this results in about 3 background alerts per year ⁸. This number is calculated taking into account that a source is on average visible with a probability of 40% by a partner observatory (i.e. if the source rises at least 30 degrees above the horizon for at least 30 minutes during dark time, the current phase of the Moon is less than 0.5 and the source distance to the Moon is larger than 60°). For VERITAS, a higher alert threshold (3.6σ) leads to one expected background alert per year.

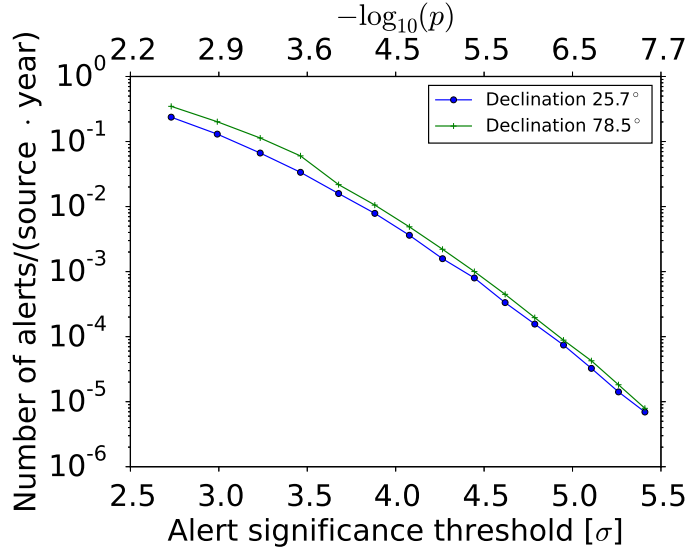


Figure 8. Expected IceCube fake alert rates for the NToO caused by atmospheric neutrinos for different source declinations as a function of alert significance.

6 Data stability monitoring

A dedicated monitoring system was implemented to minimize the rate of false alerts caused by problems with the detector itself, the data acquisition (DAQ) or the filtering software. IceCube has very extensive DAQ monitoring, and processing results which are available with a certain delay after data-taking. However, the monitoring does not provide information on the detector stability with high granularity but declares a whole run, with a usual duration of eight hours, as either *good* or *bad*. Problems such as a few strings of the detector dropping out of the data taking shortly before the end of a run do not render the data taken up to that point invalid. To ensure that alerts are issued during stable running conditions, a simple but effective online stability monitoring scheme has been developed. The scheme is based on the continuous monitoring (in 10 min time bins) of several trigger and filter event rates, representative of different event topologies from atmospheric muons and neutrinos.

⁸Since November 2013 the number of MAGIC sources was lowered to 18 and since April 2014 the alert threshold was set to 3.6σ , therefore the expected number of alerts decreased to one alert per two years.

6.1 Rate measurements and data quality assessment

The trigger rates of the detector, and the filter event rates of the online filters, are quantities that are both sensitive to problems affecting the data quality and simple to measure, record and evaluate. Trigger event rates (e.g. the SMT8) are sensitive to low-level problems, such as possible errors in the trigger configuration or an incorrect DOM calibration. Filter event rates can also be affected by these issues but, additionally, they give information about the stability of the filtering chain. Problems that affect event reconstruction or distributions of cut variables used in a filter would also change the corresponding filter event rate.

All trigger and filter event rates are measured by a central server using a dedicated software module. Events are counted in time bins of 600 seconds and the corresponding rates and time-bin meta data (e.g. start and end of the time bin) are inserted into a relational database.

This database is mirrored to the Northern Hemisphere to be easily accessible for offline studies. Storing the data in a relational database makes it convenient to retrieve any trigger and filter event rate for longer time scales such as hours or days. For each of the trigger and filter event rates approximately $5 \cdot 10^4$ measurements are recorded in the database in a full year.

The NToO selects ν_μ -induced muon tracks to detect time-variable point sources of neutrinos. Any problem that affects the detection and reconstruction of these muons would therefore have an impact on this program. Thus the inputs derived from the rate monitoring for the NToO should be related to the muon-related triggers and filters that form the basis of the neutrino event selection. The following trigger rates, filter event rates and ratios are used to check the stability:

- *Simple Multiplicity Trigger* event rate
- *Muon Filter* event rate
- *Online Level 2 Filter* rate
- Ratio of *Online Level 2 Filter* event rate to *Muon Filter* event rate
- Ratio of *Online Level 2 Filter* event rate to *Simple Multiplicity Trigger* rate

A combination of these rates and ratios form a *stability score*, which will be described in Sec. 6.2.

As the final neutrino event selection is performed in a different subsystem, the final-level event rate is not recorded in the database. Due to the very low atmospheric-neutrino rate of about 2 mHz at the final cut level, the statistical error on the rate measurement with the default time binning of 10 minutes would be very large. Recording this rate with a different binning and combining it with the other rates would make the system much more complicated. Therefore, the final neutrino level event rate is not used as an input in the rate-based detector stability monitoring.

6.2 Stability-score calculation

The atmospheric-muon rate depends on the development of the air shower and thus on the atmospheric density profile. As seasonal temperature changes of the atmosphere influence this density profile, the atmospheric-muon rate measured in the detector shows a pattern of seasonal variation,

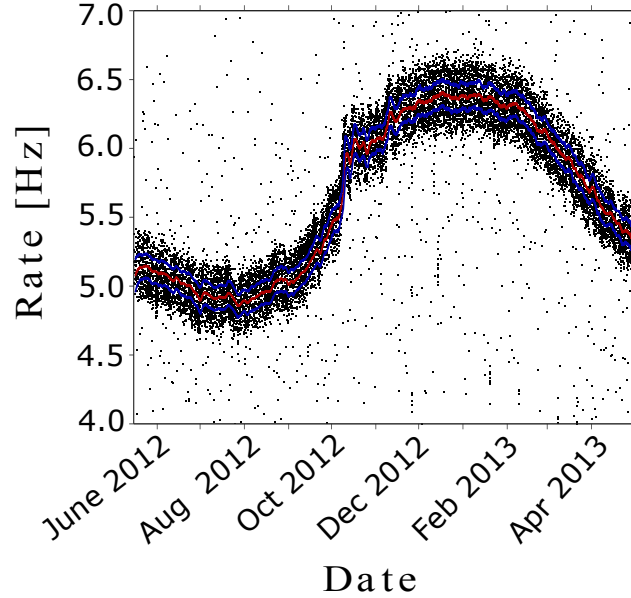


Figure 9. IceCube rate of events passing the *Online Level 2 Filter* over the complete IC-2012 season. The solid red line depicts the moving average of the *Online Level 2 Filter* event rate; the blue lines show the 1σ exponential standard deviation around the average. Each dot corresponds to a 10 min time bin.

see Figure 9. On top of these slow seasonal variations, changes in the IceCube trigger rate on the time scale of hours to days are apparent. This background of atmospheric muons dominates all trigger and filter event rates used for the online stability monitoring. Therefore, a simple stability decision based on the deviation from fixed reference rates cannot be used.

A common method to predict a time series of (potentially noisy) measurements is a moving-average filter. The filter smooths noisy data to either produce smoothed data for presentation purposes or to make forecasts of the time series. Three different averaging methods are usually employed, simple moving averages, weighted moving averages or exponential moving averages.

An N -period simple moving average weights the last N measurements equally to produce the smoothed prediction. In doing this, the average always lags sudden changes in the data. This can be overcome by applying a weight to each measurement in the averaging process, depending upon how long ago the measurement was taken. This requires two inputs, the number of measurements N to average over and the weight function. In the case of the stability monitoring one would assign higher weight to more recent measurements so that the average reacts faster to changes of the rates caused by a changing muon rate.

Another way to achieve this fast adaptation is an exponential moving average. Given measurements of a quantity x (e.g. a filter event rate) at time steps i (denoted as x_i) the exponential moving average S at time step i is calculated as

$$S_1 = x_1 \tag{6.11}$$

$$S_i = \alpha x_i + (1 - \alpha)S_{i-1} ; \text{ for } i > 1 . \tag{6.12}$$

The parameter α determines how fast the weight given to past measurements decays; higher

α gives more weight to recent observations and reduces the impact of past measurements more rapidly. The step width is given by the 600-second time-bin width of the rate monitoring.

Analogously to the exponential moving average, an exponential moving standard deviation σ can be defined as

$$\sigma_i = \sqrt{\langle x^2 \rangle - S_i \cdot S_i}. \quad (6.13)$$

Here $\langle x^2 \rangle$ denotes the exponential moving average (see Eq. 6.12) of x^2 . To update the exponential moving average only the most recent calculated value of S_i is needed. This is in contrast to the simple and weighted moving averages, where the past N data points need to be kept for updates of the average. Therefore, an exponential smoothing has been chosen in the stability monitoring in order to simplify the implementation of the moving-average calculation.

6.3 Implementation of the stability-score calculation

The stability score provides a metric to compare the current detector trigger and filter event rates in time bin i to an exponential moving average of these rates up to that point in time. The averages and standard deviations are calculated for the filter event rates and ratios with the parameters $\alpha = 0.01$ ⁹. In order to judge the detector stability in a time bin i , a combined score ξ_i is calculated as

$$\xi_i = \sum_j \frac{|x_i^j - S_{i-1}^j|}{\sigma_{i-1}^j} \quad (6.14)$$

where j enumerates the filter event rates and ratios and S_{i-1} and σ_{i-1} are the exponential moving averages and standard deviation, respectively, prior to the time bin i . If ξ_i is below a certain threshold ξ_{thresh} the time bin i is considered to be of good quality and the averages and standard deviations are updated according to Eq. 6.12 and Eq. 6.13. If ξ_i is above the threshold the data quality in this time bin is judged to be bad. In this case, all final-level events in that time bin are discarded, the time bin is counted as detector dead time and the averages and standard deviations are not updated with the rates from time bin i .

The threshold employed in the NToO is $\xi_{\text{thresh}} = 8$. For this threshold, comparisons of the online stability monitoring with the more extensive offline quality checks show that the online system reliably identifies unstable detector conditions.

As an example, for IC-2012 the data taking season started on 15 May 2012 at 10:05:48 UTC and ended on 2 May 2013 at 09:48:49 UTC. Of the 351.98 days between the season start and end, 322.17 days are marked as good by the stability monitoring. This results in an uptime fraction of 91.5%. Typical IceCube offline analyses for this season report an uptime fraction of around 95 %.

7 Technical design of the alert system

The NToO system runs online at the South Pole with minimal human intervention. In order to maximize the uptime of the system it has to be very stable. The main design driver was that the

⁹Until 25 November 2012 $\alpha = 0.005$, which gave more weight to past measurements. In order to be better able to cope with fast rate variations due to weather changes the value of α was changed to 0.01.

failure of any of the sub-components should not lead to the loss of the online program’s data. Therefore all components have been separated as much as possible and intermediate results are stored frequently. The basic components of the NToO are depicted in Figure 10.

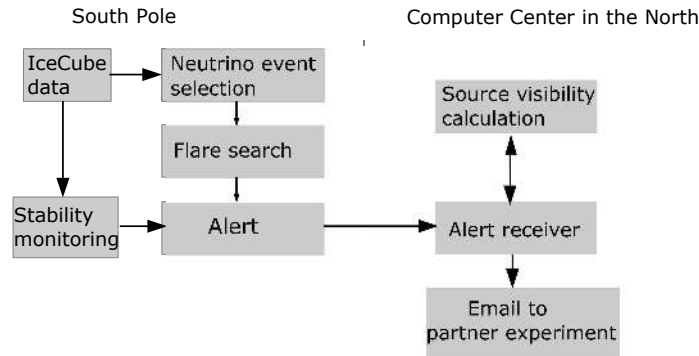


Figure 10. Schematic of the design of the IceCube NToO.

In the first step, the selection of neutrino candidate events happens inside the IceCube data-processing system at South Pole. Each event is serialized to the text-based and human-readable JSON (JavaScript Object Notation) format and written to a dedicated directory on disk. The event directory is checked for new events every 30 seconds by the daemon that runs the time-clustering algorithm. This daemon keeps a list of events detected in the last 21 days from each of the monitored sources and adds new events to the appropriate list if the detector was stable when the event was detected. For each new event that falls into the search bin of one of the monitored sources the time-clustering algorithm for that particular source is run.

If the significance for an evaluated event cluster exceeds a certain threshold (see below), an alert message containing the source name, event positions, event times and the significance of the cluster is generated. The alert message is then sent to the University of Wisconsin via the IceCube Teleport System (ITS) which uses the network of Iridium satellites. This low-bandwidth connection allows short messages to be sent from the South Pole without any significant delay. Once the message arrives in the North it is checked to see whether it represents a *real alert* or a *test alert* from a monitoring source (see next section for an explanation of the difference). If it is a *real alert*, the alert is forwarded to the respective partner experiment, MAGIC or VERITAS or to both of them if the alert significance is above the threshold for MAGIC and VERITAS. Currently the alerts are forwarded via email and follow-up observations are initiated manually. The total time delay between the (latest) neutrino event detected by IceCube and the moment that alert is forwarded to the partner experiment is on average 12 minutes.

8 Monitoring of alert system

The low rate of accidental background alerts from atmospheric neutrinos (see Figure 8) makes it necessary to add additional monitoring to the system in order to ensure that all components are working as expected. Ideally, this monitoring should cover the whole chain, from the event

selection and stability monitoring, to the generation, sending and receiving of alerts. In order to reach this goal, so-called test alerts can be generated at the South Pole using the same event sample as used by the NToO. To achieve a sufficiently large rate of test alerts the number of source positions that are monitored should be high. Thus, 1000 random positions were chosen as test sources, with a flat distribution in $\cos \theta$. The threshold for sending a test alert should be lower than the corresponding threshold for the physics alerts in order to achieve a high number of test alerts. Thus, the threshold for test alerts was set to $p_{obs} = 0.1$ (see Eq. 5.10).

Using the same original neutrino event sample for both the physics alerts and for the test alerts would unblind additional positions in the sky. The usual way to test point-source analyses in a way that preserves blindness is through scrambled data sets. The event times are shuffled and new sky coordinates are calculated for each event. Due to the location of the IceCube exactly at the geographic South Pole, only the right ascension is affected by this procedure. In the case of the NToO, however, a continuous stream of events must be shuffled while preserving properties such as the azimuth and time distribution of the events.

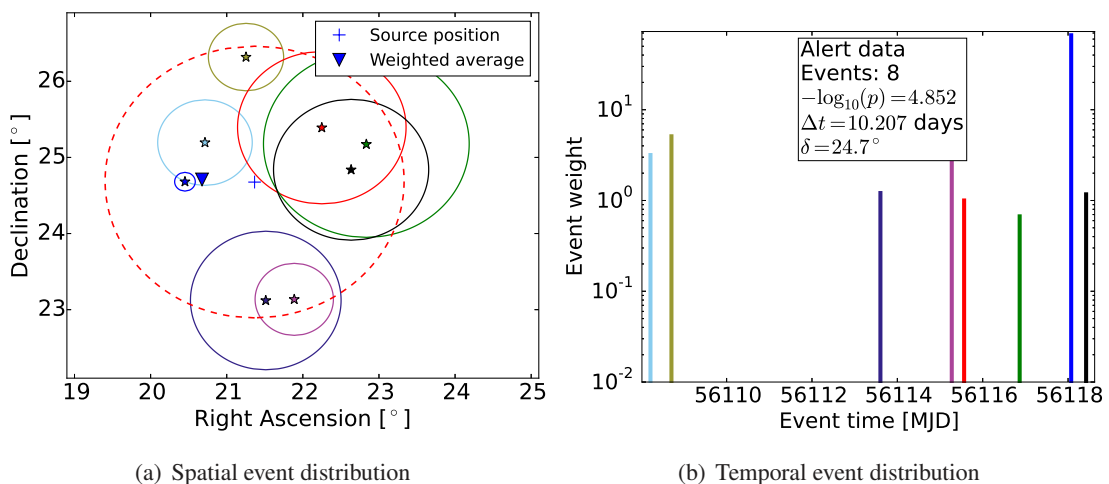


Figure 11. Left panel shows spatial distribution of IceCube events (marked by stars) contributing to a test alert. The circles describe the estimated angular error for the reconstructed tracks. The dashed circle indicates the size of the on-source bin. Right panel shows the temporal distribution of eight events depicted in the left panel. The height of the bars in right panel corresponds to the event weights derived from the angular reconstruction uncertainties. The weights are used to calculate the weighted average direction of the events, shown as an inverse full triangle in the left panel.

To randomize the event coordinates in right ascension for the blind generation of test alerts one could, in principle, assign each event a random azimuth angle. This would, however, destroy the pattern due to the azimuth-dependent efficiency of the detector, see Figure 6. In order to preserve this pattern in the scrambled dataset, the conversion of local coordinates (zenith and azimuth) to sky coordinates (right ascension and declination) for each event is done not with its original event time, but with the time of the previous neutrino event. The first event after the startup of the event-selection process is assigned a random right ascension. As the rate of atmospheric-neutrinos is about 2 mHz this results in a random shift of each event by several degrees on average.

The test alerts generated from the blinded event sample are collected and analyzed. To aid

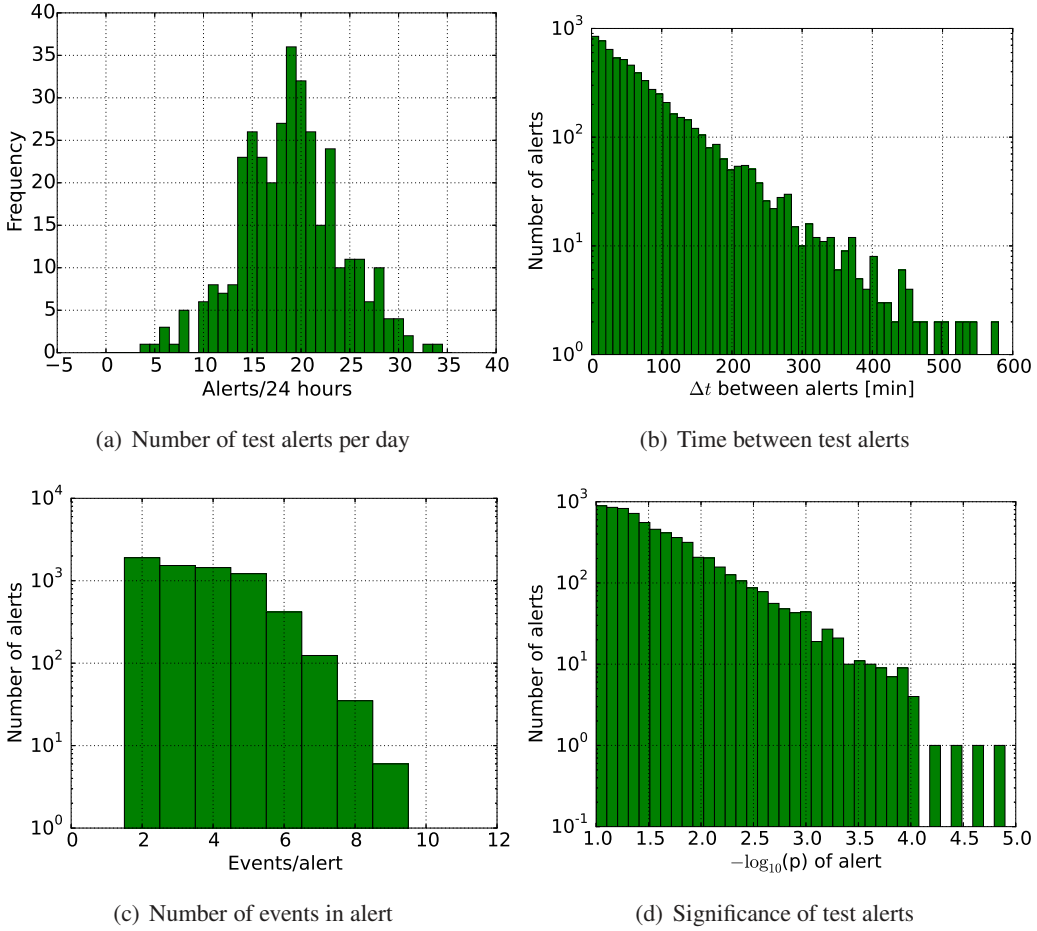


Figure 12. Monitoring information derived from the test alerts for the IceCube NToO. See text for a description.

the interpretation of these alerts a web page was created that displays each alert. The web page is automatically updated upon receiving a new test alert. In addition to each individual test alert, the global properties of all test alerts received to date are shown, e.g. the rate of test alerts, their zenith distribution and their significance distribution. Each alert is displayed on a web page showing the distribution of events contributing to the alert both in time and space (see Figure 11). In the case of an alert for an astrophysical source this allows for a rapid inspection of the event properties.

As an example, Figure 11 depicts a high-multiplicity test alert, consisting of 8 events, issued on 7 July 2012. It corresponds to the test alert with the highest significance in the IC-2012 data taking season with $-\log_{10}(p_{obs}) = 4.85$. The contributing events were detected over a duration of 10.2 days.

For each alert the weighted-average direction is calculated as

$$x_{avg} = \sum_i \frac{\sum_j \sigma_j^2}{\sigma_i^2} x_i \quad (8.15)$$

where the σ_i are the resolution estimates of the individual events (i.e. *Cramér-Rao Resolution Estimate*) and the x_i are their directions described by the right ascension and declination. The

weighted average is displayed as a full triangle in the spatial event plot, the individual event weights ($1/(\sigma_i^2 / \sum_j \sigma_j^2)$) are represented as the height of the bars in the temporal plot.

Plots of the global properties of all monitoring alerts received to date can be used to monitor the stability of the operation of the whole alert system. For example, changes in the total test-alert rate can indicate problems with the event selection or uptime calculation. Long delays between the detection of the events and the arrival of the test alerts in the North can be a sign of problems with the data processing, the stability-monitoring database or the transfer of test alerts to the North. Figure 12 shows some of the quantities derived from the test alerts which allow the alert system to be monitored.

An important quantity to monitor is the rate of received test alerts (Figure 12(a)). The regular arrival of test alerts in the North is used as a “heartbeat” for the overall system. If no test alert is received for more than six hours, a warning email is issued to a list of people so that the cause can be investigated. Warning emails are reissued every two hours if no new alert has been received in the meantime. This threshold of six hours for warning emails is rather conservative, as can be seen in Figure 12(b). This figure shows the histogram of the wait times between subsequent test alerts. It follows the expected exponential distribution reasonably well. A time difference of six hours is well within the range of expected waiting times. However, to enable timely interventions, an early warning is preferred. Figure 12(d) depicts the distribution of the significances of the test alerts.

9 Results of NToO program

The IceCube follow-up programs such as optical, X-ray follow-up and NToO have been running in a stable fashion for a few years and are taking high-quality data from both IceCube and the follow-up instruments. The results are the subject of a forthcoming publications. Only a short status report will be given here, highlighting the most important results.

For the optical and X-ray follow-up, no significant excess of multiplets was found since the inauguration of the program in December 2008. One neutrino triplet was found in the data in February 2016, this result will be subject of a forthcoming IceCube publication. In March 2012, the most significant alert during the first three years of operation of the optical and X-ray follow-up program was issued by IceCube. In the follow-up observations performed by the PTF, a Type II supernova PTF12csy was found 0.2° away from the neutrino alert direction [35]. The supernova has a redshift of $z = 0.0684$, corresponding to a luminosity distance of about 300 Mpc, and the Pan-STARRS1 survey shows that its explosion time was at least 158 days (in the host-galaxy rest frame) before the neutrino alert, implying that a causal connection is unlikely [35].

From the inauguration of the NToO program, on 14 March 2012, to 31 December 2015, 14 alerts were sent: 4 in 2012, 2 in 2013, 6 in 2014 and 2 in 2015. The program continues, and alerts during 2016 and beyond will be reported elsewhere. From the above-mentioned 14 alerts issued, 8 of those were forwarded and 4 (out of 8) were followed-up by MAGIC or VERITAS observations. Another 6 alerts (out of 14 issued) were not forwarded due to bad observing conditions or the partner experiment was not operational.

Table 4 gives an overview of all of the alerts generated by the NToO up to 31 December 2015. Below, only the alerts forwarded to the partner experiments are discussed in more detail.

alert ID	Source	Time (UTC)	$-\log_{10}(p_{\text{obs}})$	N_{obs}	Duration (days)	Follow-up Instrum.	Observed yes/no
1	PG 1424+240* ^{**}	2012-04-14 23:47	3.47	6	7.617	No	-
2	GB6 B1310+4844	2012-08-20 09:53	3.75	6	6.344	No	-
3	4C15.54	2012-09-13 01:52	4.06	2	0.001	MAGIC	No
4	SBS 1150+497 ^{**}	2012-11-09 07:28	4.64	6	4.169	VERITAS	Yes
5	RGB J0152+017 [*]	2013-04-29 06:36:	4.07	8	15.801	No	-
6	RGB J0505+612 ^{**}	2013-09-12 20:00	3.31 (4.10)	7 (10)	11.790 (20.73)	MAGIC	Yes
7	1ES 2344+514 [*]	2014-02-19 23:18	4.07 (4.23)	8 (9)	12.844 (16.40)	VERITAS	Yes
8	1ES 1959+650 [*]	2014-03-09 10:28	3.40	9	20.944	MAGIC	No
9	B3 1708+433	2014-06-22 02:42	4.34	3	0.118	No	-
10	PKS 1717+177 ^{**}	2014-09-24 13:47	3.20	2	0.007	No	-
11	MG4 J200112+4352 [*]	2014-10-05 15:05	4.05	9	18.631	VERITAS	Yes
12	B3 1343+451	2014-11-16 17:00	3.64 (5.04)	3 (4)	0.301 (0.576)	VERITAS	No
13	AO 0235+164 ^{**}	2015-04-27 04:55	3.97	8	16.395	No	-
14	CGRaBS J0211+1051 ^{**}	2015-07-05 00:06	4.09	4	1.205	VERITAS	No

Table 4. Overview of the IceCube alerts generated by the NToO up to 31 December 2015; see text for more details. Time of alert corresponds to the time when alert was received at North. (Follow-up Instrum.= Follow-up Instruments; Numbers in brackets correspond to the followed alert during the next few days, * - known VHE source, ** - existing VHE limit in [77]).

The most interesting alert (alert #4 in Table 4) was generated on 9 November 2012, consistent with position of the source SBS 1150+497 (located at zenith angle $\theta = 139.5^\circ$, with respect to IceCube). The alert comprised six events observed during 4.169 days. The spatial and temporal distribution of these events is shown in Figure 13. The Poisson probability (pre-trial) for this observation is $-\log_{10}(p_{\text{obs}}) = 4.64$, the post-trial probability $-\log_{10}(p_{\text{obs}}) = 2.60$, making it the most significant alert sent during this IceCube season (IC-2012). The alert was forwarded to the VERITAS collaboration and resulted in a follow-up observation. Due to poor weather and bright moonlight conditions, VERITAS observations were not possible until 12 November 2012, at which point the source was visible at low elevation at the very end of the night. A further observation was made on the following night giving a total exposure time of 71.5 min. No evidence for gamma-ray emission was seen from the position of the source, giving an integral flux upper limit (99% confidence) above 300 GeV of $3.0 \times 10^{-10} \text{ cm}^{-2}\text{s}^{-1}$ for an assumed differential spectrum with spectral index $\gamma = 2.5$.

Another high-significance alert was sent to VERITAS on 19 February 2014, followed by a second alert on 23 February 2014, spatially coincident with the source 1ES 2344+514 (alert #7). The first of these was triggered by 8 neutrinos observed over a period of 12.844 days, with $-\log_{10}(p_{\text{obs}}) = 4.07$. An additional event, observed 3.6 days later, increased the p -value to $-\log_{10}(p_{\text{obs}}) = 4.23$, the post-trial probability $-\log_{10}(p_{\text{obs}}) = 2.31$, which resulted in the second forwarded alert for this source. The source was barely visible to VERITAS (zenith angle $> 60^\circ$), and weather conditions were poor. The online VERITAS analysis showed no evidence for gamma-ray emission (no excess was detected), indicating that the source flux was likely not exceptionally high above a few TeV.

During the next IceCube season (IC-2014) another two alerts were sent to VERITAS. The

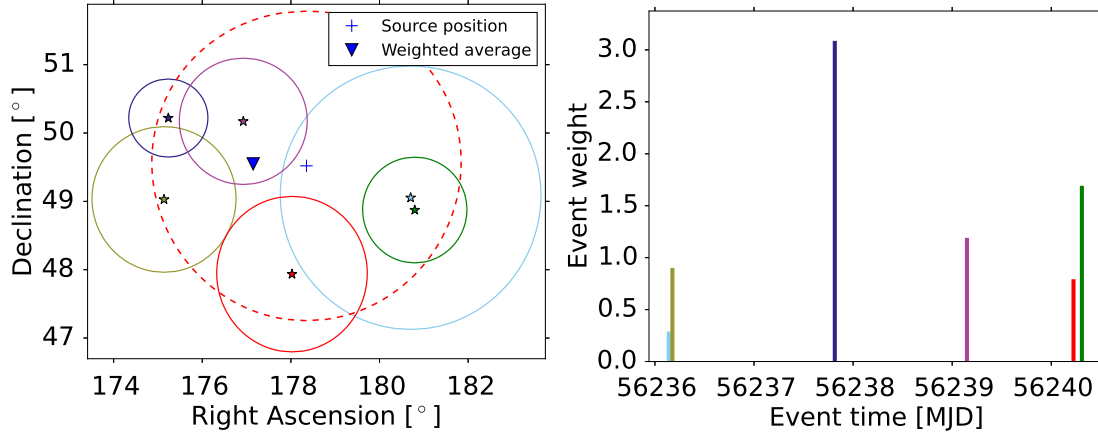


Figure 13. Left panel shows position of events (star symbols) and related uncertainty (circles) from the alerts that were sent to VERITAS on 2012 November 9. The weighted average of the contributing events is calculated using an event-by-event angular resolution estimator. The dashed circle indicates the size of the on-source bin. Right panel shows the temporal distribution of eight events depicted in the left panel.

first, generated on 5 October 2014 corresponded to the source MG4 J200112+4352 (alert #11), which had been recently reported as VHE emitter by the MAGIC collaboration [78]. A one-hour observation was performed, but under extremely poor weather and bright moonlight conditions. No conclusion regarding the gamma-ray flux state is possible with these data. The second alert was issued by the NToO system for the source B3 1343+451 on 16 November 2014 (alert #12), but the source was again barely visible (zenith angle larger than 60°) and so follow-up observations were not performed. The last alert was sent to VERITAS on 5 July 2015 for the source CGRaBS J0211+1051 (alert #14), but at this time VERITAS was undergoing its annual summer shutdown, and so no observation was made.

For MAGIC, the first alert was sent on 14 April 2012, spatially coincident with the source 4C15.54 (alert #3). However, as the MAGIC telescope was in a commissioning phase, the alert could not be followed up. Then, a series of four alerts were issued by the NToO from 12 September 2013 to 21 September 2013 for the source RGB J0505+612 (alert #6). The alert resulted in a follow-up observation by MAGIC (1 hour), which showed no statistically significant evidence for gamma-ray emission. The computed integral flux upper limit (99% confidence) at energies >200 GeV is $1.57 \times 10^{-11} \text{ cm}^{-2}\text{s}^{-1}$. The last alert forwarded to MAGIC was generated on 9 March 2014 for the source 1ES 1959+650 (alert #8), but the low elevation of the source precluded observations.

10 Recent and upcoming improvements

The currently deployed neutrino event selection in the NToO employs simple cuts on a number of variables that discriminate between signal neutrinos and the atmospheric-muon background. The cuts on these parameters have been optimized to achieve best sensitivity. However, further improvements in signal and background separation should be possible through the use of more sophisticated discrimination algorithms, such as boosted decision tree (BDT) [79] and multivariate learning machines. The aim is to replace the present NToO selection by developing a new event

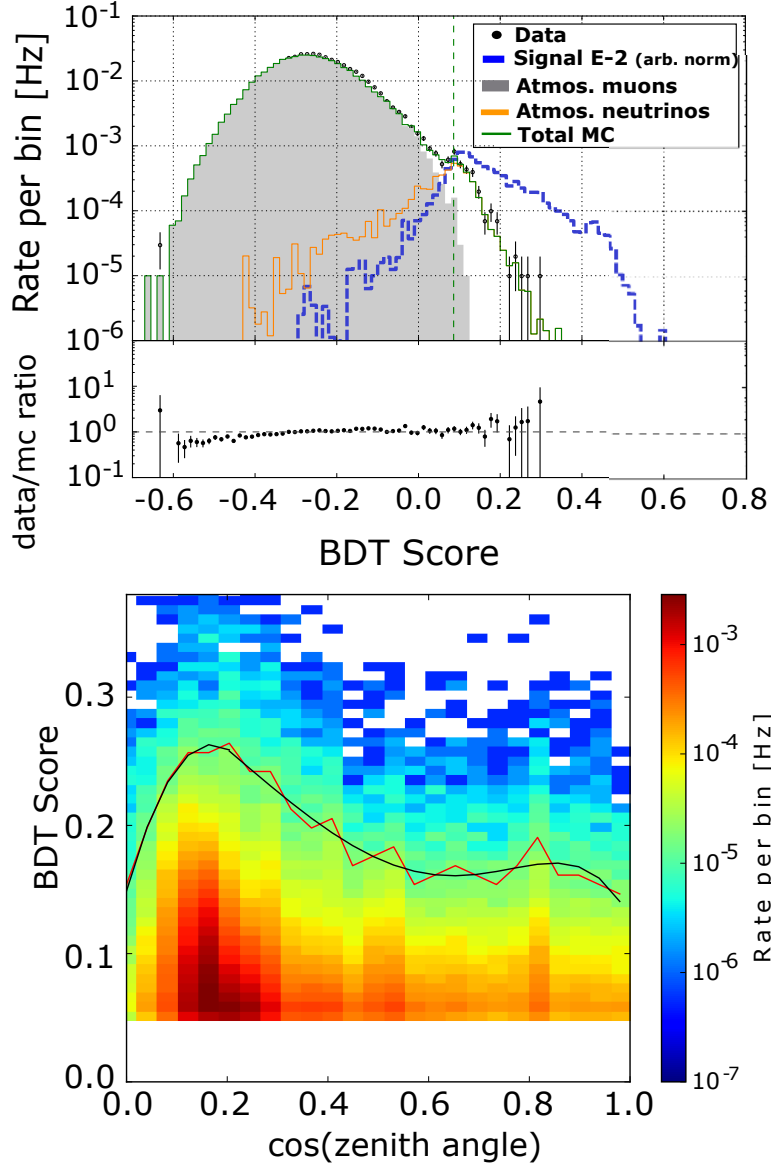


Figure 14. (Upper panel) IceCube distribution of BDT score for the ensemble of trees trained with an E^2 spectrum. Vertical dashed line corresponds to the optimized BDT cut (Northern Hemisphere). (Lower panel) The BDT score as a function of $\cos(\text{zenith angle})$. The red line keeps approximately an equal rate per zenith bin ($\approx 10^{-4}$ Hz). A piecewise polynomial function is then fitted to the red curve (black curve).

selection, which could also be used by other IceCube follow-up programs. This new event selection is comparable to offline point-source samples and will cover the entire sky. Here, a short description of the new BDT selection is presented, which has been implemented for the IC-2015 data-acquisition season.

For the new BDT selection scheme, the multivariate cuts were based on 14 observables obtained by choosing parameters with low correlation in the background event sample, but with high discriminating power between signal and background. Observables specifying the geometry and time evolution of the hit pattern, as well as the quality and consistency of the various track re-

Cut Level	Data rate (mHz)	Atm. ν_μ rate (mHz)	E^{-1} Eff. (%)	E^{-2} Eff. (%)	$E^{-2.7}$ Eff. (%)
Northern Hemisphere					
Simple Cuts	2.0	1.9	79	69	54
BDT $E^{-2.0}$	1.9	1.7	86	81	72
Southern Hemisphere					
BDT $E^{-2.0}$	2.1	0.06	78	45	35

Table 5. Data and atmospheric neutrino muon for different cut progression in IceCube. The signal efficiency for an E^{-2} neutrino spectrum and for well reconstructed events with $\Delta\Psi < 5^\circ$ with respect to the *Online Level 2 Filter* is also shown.

constructions and the number of strings with signals are used. The BDT training was done with simulated signal events for a soft neutrino spectrum of $E^{-2.7}$ and for an E^{-2} spectrum. As an example, Figure 14 depicts results of the BDT training for an E^{-2} spectrum. A set of real data provided the background sample for training. Additionally, for the simulated signal, the reconstructed track was required to be within of 5° of the simulated direction in order to train the BDTs with only well-reconstructed events. The final selection cut on the BDT output variable was optimized to provide the best discovery potential for an E^{-2} neutrino flux, which results in a BDT score value of 0.106. This final cut leads to a rate of 2 mHz for the final sample and, as shown in Table 5, to a better signal efficiency (with respect to *Online Level 2 Filter* efficiency) than the original NToO cuts. The BDT-based event selection leads to an improvement in the signal efficiency of about +12(+18)% for an E^{-2} ($E^{-2.7}$) spectrum with respect to the simple cuts.

The BDT selection was also used for the Southern Hemisphere (zenith angle $\theta < 90^\circ$). However, instead of a single BDT-score cut value, a zenith-dependent cut was applied in order to select a constant number of events per solid angle, as shown in Figure 14 (Lower panel). This zenith-dependent cut was also optimized with respect to sensitivity and discovery potential for an E^{-2} neutrino spectrum. The optimized cut described by a polynomial fit (Figure 14 (Lower panel)) leads to a total data rate of 2.1 mHz for the South only and an average signal efficiency of about 45 % (with respect to the *Online Level 2 Filter*), see also Table 5.

The first step in establishing the NToO program was to demonstrate its technical feasibility and to prove that a time-dependent point-source search can be run stably and reliably over long periods of time at the South Pole. Therefore a simple search technique like the binned method was implemented first. However, current offline IceCube searches for neutrino point sources usually employ unbinned maximum-likelihood methods [80] to increase the discovery potential. Such an approach has now also been implemented for the NToO ¹⁰, which allows the alert significance to be calculated by taking into account an event-by-event angular reconstruction uncertainty estimation and an energy estimation of the event.

Upgrading the NToO with a BDT-based event selection and a subsequent likelihood analysis leads to an increased sensitivity in the Northern Hemisphere of 30-40%, yielding a comparable sensitivity to the standard offline point-source analysis [81]. It also opens up the possibility of

¹⁰ At the moment the unbinned maximum likelihood is implemented as a standalone cpython module, which will be included in the next forthcoming upgrade of the NToO system.

observing neutrino flares in the Southern Hemisphere and to forward these alerts to the H.E.S.S. collaboration [10], with whom a memorandum of understanding has been established.

In previous years of operation of the NToO systems, neutrino candidate event selections, multiplet selection and alert generation all took place within the data-acquisition system at the South Pole. This system was found to be somewhat inflexible and difficult to expand. To address these shortcomings, the NToO systems are currently transitioning to a new approach. Instead of selecting the neutrino candidates at the South Pole, a BDT-selected stream of single high-quality neutrino events is transmitted to the North via a rapid satellite communication channel. Follow-up processes in the North now evaluate the neutrino candidates, and generate alerts for external observatories; see [81] for a more detailed description. Until December 2015, alerts were sent to the partner experiments privately. However, in the future we plan to distribute alerts to the full multi-messenger astrophysics community (ANTARES, KM3NeT, Auger, H.E.S.S./CTA, LIGO/VIRGO, etc.) via the Astrophysical Multimessenger Observatory Network (AMON) [82].

11 Summary and Conclusions

In this work we described a NToO program, which uses IceCube to monitor a list of predefined source candidates for neutrino flares. An important goal of this program was to establish and to test procedures to trigger promptly the gamma-ray community to collect sensitive VHE data from specific sources during periods of time when IceCube measures a potential increase in their neutrino flux. These periods of elevated emission (“flares”), both in gamma rays and neutrinos, are of particular interest to identify the sources of astrophysical neutrinos, and to understand the source emission mechanisms. The second goal of the NToO is to increase the discovery potential for time-variable point-sources of neutrinos with IceCube. The detection of a high-energy gamma-ray flare with an IACT triggered by an alert from IceCube can help to establish the neutrino signal, even if it is not significant enough on its own to qualify as a discovery. The NToO is the first online analysis in IceCube searching for neutrino flares from point sources on time scales longer than a few minutes. We have shown that such an analysis can be done efficiently and reliably, and presented the first results from this program.

Acknowledgments

We acknowledge the support from the following agencies: U.S. National Science Foundation-Office of Polar Programs, U.S. National Science Foundation-Physics Division, University of Wisconsin Alumni Research Foundation, the Grid Laboratory Of Wisconsin (GLOW) grid infrastructure at the University of Wisconsin - Madison, the Open Science Grid (OSG) grid infrastructure; U.S. Department of Energy, and National Energy Research Scientific Computing Center, the Louisiana Optical Network Initiative (LONI) grid computing resources; Natural Sciences and Engineering Research Council of Canada, WestGrid and Compute/Calcul Canada; Swedish Research Council, Swedish Polar Research Secretariat, Swedish National Infrastructure for Computing (SNIC), and Knut and Alice Wallenberg Foundation, Sweden; German Ministry for Education and Research (BMBF), Deutsche Forschungsgemeinschaft (DFG), Helmholtz Alliance for Astroparticle Physics (HAP), Research Department of Plasmas with Complex Interactions (Bochum),

Germany; Fund for Scientific Research (FNRS-FWO), FWO Odysseus programme, Flanders Institute to encourage scientific and technological research in industry (IWT), Belgian Federal Science Policy Office (Belspo); University of Oxford, United Kingdom; Marsden Fund, New Zealand; Australian Research Council; Japan Society for Promotion of Science (JSPS); the Swiss National Science Foundation (SNSF), Switzerland; National Research Foundation of Korea (NRF); Villum Fonden, Danish National Research Foundation (DNRF), Denmark.

The VERITAS Collaboration acknowledges the support of the U.S. Department of Energy Office of Science, the U.S. National Science Foundation and the Smithsonian Institution, and NSERC in Canada. We also acknowledge the excellent work of the technical support staff at the Fred Lawrence Whipple Observatory and at the collaborating institutions in the construction and operation of the instrument.

The MAGIC collaboration would like to thank the Instituto de Astrofísica de Canarias for the excellent working conditions at the Observatorio del Roque de los Muchachos in La Palma. The financial support of the German BMBF and MPG, the Italian INFN and INAF, the Swiss National Fund SNF, the ERDF under the Spanish MINECO (FPA2015-69818-P, FPA2012-36668, FPA2015-68278-P, FPA2015-69210-C6-2-R, FPA2015-69210-C6-4-R, FPA2015-69210-C6-6-R, AYA2013-47447-C3-1-P, AYA2015-71042-P, ESP2015-71662-C2-2-P, CSD2009-00064), and the Japanese JSPS and MEXT is gratefully acknowledged. This work was also supported by the Spanish Centro de Excelencia “Severo Ochoa” SEV-2012-0234 and SEV-2015-0548, and Unidad de Excelencia “María de Maeztu” MDM-2014-0369, by grant 268740 of the Academy of Finland, by the Croatian Science Foundation (HrZZ) Project 09/176 and the University of Rijeka Project 13.12.1.3.02, by the DFG Collaborative Research Centers SFB823/C4 and SFB876/C3, and by the Polish MNiSzW grant 745/N-HESS-MAGIC/2010/0.

References

- [1] T.K. Gaisser and T. Stanev, *Neutrinos and cosmic rays*, *Astroparticle Physics* **39-40** (2012) 120.
- [2] K. Koyama et al., *Evidence for shock acceleration of high-energy electrons in the supernova remnant SN1006*, *Nature* **378** (1995) 255.
- [3] A.M. Atoyan and C. Dermer, *Neutrinos and γ -rays of hadronic origin from AGN jets*, *New Astronomy Reviews* **48** (2004) 381.
- [4] A. Neronov and M. Ribordy, *IceCube sensitivity for neutrino flux from Fermi blazars in quiescent states*, *Physic Review D* **80** (2009) 083008.
- [5] A. Mucke et al., *BL Lac objects in the synchrotron proton blazar model*, *Astroparticle Physics* **18** (6) (2003) 593.
- [6] M.G. Aartsen et al. (IceCube Collaboration), *An All-Sky Search for Three Flavors of Neutrinos from Gamma-Ray Bursts with the IceCube Neutrino Observatory*, *The Astrophysical Journal* **824:115** (2016) 13.
- [7] M.G. Aartsen et al. (IceCube Collaboration), *Evidence for High-Energy Extraterrestrial Neutrinos at the IceCube Detector*, *Science* **342** (2013) 1242856.
- [8] L.A. Anchordoqui et al., *Cosmic neutrino pevatrons: A brand new pathway to astronomy, astrophysics, and particle physics*, *Journal of High Energy Astrophysics* **1-2** (2014) 1.

- [9] VERITAS Collaboration: <http://veritas.sao.arizona.edu/>.
- [10] HESS Collaboration: <http://www.mpi-hd.mpg.de/hfm/HESS/>.
- [11] MAGIC Collaboration: <http://http://magic.mppmu.mpg.de/>.
- [12] M. Santander, for the VERITAS, IceCube Collaborations, *Searching for TeV gamma-ray emission associated with IceCube high-energy neutrinos using VERITAS*, Proc. 34th International Cosmic Ray Conference (ICRC), The Hague, 2015 [arXiv:1509.00517].
- [13] F. Schussler et al. for the HESS Collaboration, *The H.E.S.S. multi-messenger program*, Proc. 34th International Cosmic Ray Conference (ICRC), The Hague, 2015 [arXiv:1509.03035].
- [14] M. Petropoulou, S. Coenders, S. Dimitrakoudis, *Time-dependent neutrino emission from Mrk 421 during flares and predictions for IceCube*, *Astroparticle Physics* **80** (2016) 115.
- [15] M.G. Aartsen et al. (IceCube Collaboration), *Searches for extended and point-like neutrino sources with four years of IceCube data*, *The Astrophysical Journal* **796** (2014) 109.
- [16] M.G. Aartsen et al. (IceCube Collaboration), *Searches for time dependent neutrino sources with IceCube data from 2008 to 2012*, *The Astrophysical Journal* **807** (2015) 46.
- [17] F. Aharonian et al., *The time averaged TeV energy spectrum of Mkn 501 of the extraordinary 1997 outburst as measured with the stereoscopic Cherenkov telescope system of HEGRA*, *Astronomy and Astrophysics* **349** (1999) 11.
- [18] J. Albert et al. (MAGIC Collaboration), *Variable VHE gamma-ray emission from Markarian 501*, *The Astrophysical Journal* **669** (2007) 862.
- [19] F. Aharonian et al., *Variations of the TeV energy spectrum at different flux levels of Mkn 421 observed with the HEGRA system of Cherenkov telescopes*, *Astronomy and Astrophysics* **393** (2002) 89.
- [20] I. Donnarumma et al., *The June 2008 flare of Markarian 421 from optical to TeV energies*, *The Astrophysical Journal* **691** (2009) L13.
- [21] F. Aharonian et al., *An Exceptional Very High Energy Gamma-Ray Flare of PKS 2155-304*, *The Astrophysical Journal*, **664** (2007) L71.
- [22] J. Aleksic et al. (MAGIC Collaboration), *The major upgrade of the MAGIC telescopes, Part II: A performance study using observations of the Crab Nebula*, *Astroparticle Physics* **72** (2016) 76.
- [23] N. Park for the VERITAS Collaboration, *Performance of the VERITAS experiment*, Proc. 34th International Cosmic Ray Conference (ICRC), The Hague, 2015 [arXiv:1508.07070].
- [24] M. Ackermann et al. (IceCube Collaboration), *The IceCube Collaboration: contributions to the 29th International Cosmic Ray Conference (ICRC 2005), Pune, India, Aug. 2005*, Proc. 29th International Cosmic Ray Conference (ICRC), The Pune, 2005 [arXiv:astro-ph/0509330].
- [25] M. Ackermann et al. (The IceCube Collaboration), *The IceCube Neutrino Observatory - Contributions to ICRC 2015 Part I: Point Source Searches*, Proc. 34th International Cosmic Ray Conference (ICRC), The Hague, 2015 [arXiv:1510.05222 p. 21].
- [26] R. Franke, *Design, implementation and first results of the Neutrino Triggered Target of Opportunity Program with the IceCube neutrino telescope*, PhD thesis Humboldt University (2015) <http://edoc.hu-berlin.de/docviews/abstract.php?lang=&id=41918>.
- [27] E. Waxman and J. Bahcall, *High Energy Neutrinos from Cosmological Gamma-Ray Burst Fireballs*, *Journal Physic Review Letter* **78** (1997) 2292.

- [28] S. Ando and J.F. Beacom, *Revealing the Supernova-Gamma-Ray Burst Connection with TeV Neutrinos*, Physic Review Letter **95** (2005) 061103.
- [29] M. Aartsen et al. (IceCube Collaboration), *Optical and X-ray follow-up programs of IceCube*, Proc. 33rd International Cosmic Ray Conference (ICRC), Rio de Janeiro, 2013 [arXiv:1309.6979 p. 40].
- [30] R. Abbasi et al. (IceCube Collaboration), *Searching for soft relativistic jets in core-collapse supernovae with the IceCube optical follow-up program*, Astronomy and Astrophysics **539** (2012) A60.
- [31] C.W. Akerlof, R.L. Kehoe, T.A. McKay et al., *The ROTSE-III Robotic Telescope System*, Publications of the Astronomical Society of the Pacific **115** (2003) 132.
- [32] N. Law, S. Kulkarni, R. Dekany et al., *The Palomar Transient Factory: System Overview, Performance, and First Results*, Publications of the Astronomical Society of the Pacific **121** (2009) 1395.
- [33] N. Gehrels, G. Chincarini, P. Giommi et al., *The Swift gamma-ray burst mission*, The Astrophysical Journal **611** (2004) 1005.
- [34] P. Evans et al., *Swift follow-up of IceCube triggers, and implications for the Advanced-LIGO era*, Monthly Notices of the Royal Astronomical Society **448** 3 (2015) 2210.
- [35] M. Aartsen et al. (IceCube Collaboration), *Detection of a Type II In Supernova in Optical Follow-up Observations of IceCube Neutrino Events*, The Astrophysical Journal **811** (2015) 52.
- [36] P.L. Nolan et al., *Fermi Large Area Telescope Second Source Catalog*, The Astrophysical Journal Supplement Series **199:31** (2012) 46; <http://heasarc.gsfc.nasa.gov/W3Browse/fermi/fermilpsc.html>.
- [37] F. Acero et al., *Fermi Large Area Telescope Third Source Catalog*, arXiv:1501.02003; http://fermi.gsfc.nasa.gov/ssc/data/access/lat/4yr_catalog/.
- [38] M. Ackermann et al., *2FHL: The Second Catalog of Hard Fermi-LAT Sources*, The Astrophysical Journal Supplement Series **222:5** (2016) 19; <https://heasarc.gsfc.nasa.gov/W3Browse/all/fermifhl.html>.
- [39] http://fermi.gsfc.nasa.gov/ssc/data/access/lat/msl_lc/.
- [40] M.L. Ahnen et al., *Very-high-energy gamma-rays from the Universe's middle age: detection of the $z=0.940$ blazar PKS 1441+25 with MAGIC*, The Astrophysical Journal Letters **815:L23** (2015) 8.
- [41] C. Urry and P. Padovani, *Unified Schemes for Radio-Loud Active Galactic Nuclei*, Publications of the Astronomical Society of the Pacific **107** (1995) 803.
- [42] M. Bottcher *Leptonic and Hadronic Modeling of Fermi-Detected Blazars*, The Astrophysical Journal **768** (2013) 54.
- [43] G. Fossati et al., *A unifying view of the spectral energy distributions of blazars* 1998, Monthly Notices of the Royal Astronomical Society **299** (1998) 433.
- [44] M. Bottcher and C. Dermer, *An evolutionary scenario for blazar unification*, The Astrophysical Journal **564** (2002) 86.
- [45] A. Cavaliere and V. D'Elia, *The Blazar Main Sequence*, The Astrophysical Journal **571** (2002) 226.
- [46] A. Abdo et al., *The Spectral Energy Distribution of Fermi bright blazars*, The Astrophysical Journal **716** (2010) 30.
- [47] M. Stickel et al., *The complete sample of 1 Jansky BL Lacertae objects. I - Summary properties*, The Astrophysical Journal **374** (1991) 431.

- [48] A.U. Abeysekara et al., *Gamma rays from the quasar PKS 1441+25: story of an escape*, The Astrophysical Journal Letters **815** (2015) L22.
- [49] J. Sitarek et al., *Detection of very-high-energy gamma rays from the most distant and gravitationally lensed blazar QSO B0218+357 using the MAGIC telescope system*, Proc. of the 34th International Cosmic Ray Conference, The Hague, 2015 [arXiv:1508.04580].
- [50] K. Satalecka et al. for the IceCube Collaboration, *Cluster Search for neutrino flares from pre-defined directions*, Proc. 30th International Cosmic Ray Conference, Merida, 2007 [arXiv:0711.0353v1].
- [51] M. Aarsten et al. (IceCube Collaboration), *Energy Reconstruction Methods in the IceCube Neutrino Telescope*, Journal of Instrumentation **9** (2014) P03009.
- [52] T. Neunhoffer, *Estimating the angular resolution of tracks in neutrino telescopes based on a likelihood analysis*, Astroparticle Physics **25** (2006) 220.
- [53] H. Cramer, Mathematical Methods of Statistics, Princeton Univ. Press and C. R. Rao, *Information and the accuracy attainable in the estimation of statistical parameters*, Bulletin of the Calcutta Mathematical Society **37** (1945) 81.
- [54] A. Achterberga et al. (IceCube Collaboration), *First year performance of the IceCube neutrino telescope*, Astroparticle Physics **26** (2006) 155.
- [55] R. Abbasi et al. (IceCube Collaboration), *The IceCube data acquisition system: Signal capture, digitization, and timestamping*, Nuclear Instruments and Methods A **601** (2009) 294.
- [56] R. Abbasi et al. (IceCube Collaboration), *Calibration and characterization of the IceCube photomultiplier tube*, Nuclear Instruments and Methods in Physics Research Section A **618** (2010) 139.
- [57] M. Aarsten et al. (IceCube Collaboration), *Muon track reconstruction and data selection techniques in AMANDA*, Nuclear Instruments and Methods in Physics Research Section A **524** (2004) 169.
- [58] M. Aarsten et al. (IceCube Collaboration), *Improvement in fast particle track reconstruction with robust statistics*, Nuclear Instruments and Methods in Physics Research Section A **736** (2014) 143.
- [59] F. James and M. Roos, *Minuit - a system for function minimization and analysis of the parameter errors and correlations*, Computer Physics Communications **10** Issue 6 (1975) 343.
- [60] J. Kennedy and R. Eberhart, *Particle Swarm Optimization*. Proceedings of IEEE International Conference on Neural Networks IV. (1995) pp. 1942-1948. doi:10.1109/ICNN.1995.488968.
- [61] G. C. Hill, *Bayesian event reconstruction and background rejection in neutrino detectors*, Proc. 27th International Cosmic Ray Conference, Hamburg, **Vol. 3** (2001) 1279.
- [62] T. R. de Young and G. C. Hill for the AMANDA Collaboration, *Application of Bayesian Statistics to Muon Track Reconstruction in AMANDA*, Proceedings of the Conference On Advanced Statistical Techniques In Particle Physics, Durham, UK, 18-22 March (2002) 235-241.
- [63] J. Ahrens et al., *Observation of High Energy Atmospheric Neutrinos with the Antarctic Muon and Neutrino Detector Array*, Physic Review **D66** (2002) 012005.
- [64] D. Heck, et al., *Corsika: A monte carlo code to simulate extensive air shower*, Wissenschaftliche Berichte FZKA 6019, Forschungszentrum Karlsruhe, 1998. <http://www-ik.fzk.de/corsika/>.
- [65] J.R. Hoerandel, *On the knee in the energy spectrum of cosmic rays*, Astroparticle Physics **19** (2003) 193.
- [66] J. Engel et al., *Nucleus-nucleus collisions and interpretation of cosmic-ray cascades*, Phys. Rev. D. **46** (1992) 5013.

- [67] A. Gazizov and M. Kowalski, *ANIS: High energy neutrino generator for neutrino telescopes*, Computer Physics Communications **172** (2005) 203.
- [68] J.H. Koehne et al., *PROPOSAL: A tool for propagation of charged leptons*, Computer Physics Communications **184** (2013) 2070
- [69] T. DeYoung, *IceTray: A software framework for IceCube*, Int. Conf. on Comp. in High-Energy Phys. and Nucl. Phys. (CHEP2004) (2005) 463.
- [70] M. G. Aartsen et al., (IceCube Collaboration), *A combined maximum-likelihood analysis of the high-energy astrophysical neutrino flux measured with IceCube*, The Astrophysical Journal **809** (2015) 98.
- [71] M. Honda, T. Kajita, K. Kasahara, S. Midorikawa, and T. Sanuki, *Calculation of atmospheric neutrino flux using the interaction model calibrated with atmospheric muon data*, Physic Review D **75** (2007) 043006.
- [72] A.R. Bell, *The acceleration of cosmic rays in shock fronts-I.*, Monthly Notices of the Royal Astronomical Society **182** (1978) 147.
- [73] R. Schlickeiser, *Cosmic-ray transport and acceleration. I - Derivation of the kinetic equation and application to cosmic rays in static cold media. II - Cosmic rays in moving cold media with application to diffusive shock wave acceleration*, The Astrophysical Journal **336** (1989) 243.
- [74] M. Mandelartz and M. J. Becker Tjus, J. 2013, *A statistical study of Galactic SNR source spectra detected at GeV energies*, (2013) [arXiv:1301.2437]
- [75] M.D. Kistler and J.F. Beacom, *Guaranteed and prospective Galactic TeV neutrino sources*, Physic Review D **74** (2006) 063007.
- [76] F. Vissani, *Neutrinos from galactic sources of cosmic rays with known gamma-ray spectra*, Astroparticle Physics **26** (2006) 310.
- [77] S. Archambault et al., *Upper limits from five years of blazar observations with the VERITAS Cherenkov telescopes*, 2016 [arXiv:1603.02410].
- [78] J. Aleksic et al., *First broadband characterization and redshift determination of the VHE blazar MAGIC J2001+439*, Astronomy and Astrophysics **572** (2014) A121.
- [79] S.S. Kerthi et al., *Improvements to Platt's SMO Algorithm for SVM Classifier Design.*, Neural Comp. **13** (2001) 637.
- [80] J. Braun, M. Baker, J. Dumm et al., *Time-Dependent Point Source Search Methods in High Energy Neutrino Astronomy*, Astroparticle Physics **33** (2010) 175.
- [81] M.G. Aarsten et al. (IceCube Collaboration), *The IceCube Neutrino Observatory - Contributions to ICRC 2015 Part I: Point Source Searches*, Proc. 34th International Cosmic Ray Conference, The Hague , 2015 [arXiv:1510.05222 p.45].
- [82] M.W.E. Smith et al., *The Astrophysical Multimessenger Observatory Network (AMON)*, Astroparticle Physics **45** (2013) 56 [arXiv:1211.5602].

12 Appendix

List of sources used by NToO for IC-2012 season (Table 6) and for IC-2013 and IC-2014 season (Table 7). In the table the source name, the declination (DEC), the right ascension (RA), search bin

radius, and threshold for sending alerts is listed. The last column indicates if the source belongs only to the MAGIC list or VERITAS list or if the source is present in the list for both experiments (BOTH).

L.P.	Source	DEC (deg)	RA (deg)	Search radius (deg)	Threshold (σ)	Exper.
1	PMN J0948+ 0022	0.3740	147.2390	1.21	3.63	VERITAS
2	BL 0414+ 009	1.0900	64.2187	1.23	3.16	BOTH
3	PKS B0906+ 015	1.3600	137.2920	1.23	3.63	VERITAS
4	RGB J0152+ 017	1.7779	28.1396	1.24	3.63	VERITAS
5	3C 273	2.0525	187.2779	1.25	3.16	BOTH
6	BL 0323+ 022	2.4208	51.5583	1.26	3.16	MAGIC
7	MG1 J050533+ 0415	4.2650	76.3950	1.30	3.63	VERITAS
8	J123939+ 044409	4.7000	189.9000	1.31	3.63	VERITAS
9	HESS J0632+ 057	5.8056	98.2429	1.34	3.63	VERITAS
10	1 ES 1212+ 078	7.5347	183.7958	1.38	3.16	MAGIC
11	4C + 09.57	9.6300	267.8900	1.43	3.63	VERITAS
12	PKS 0754+ 100	9.9400	119.3100	1.44	3.63	VERITAS
13	PKS 1502+ 106	10.4940	226.1040	1.46	3.63	VERITAS
14	CGRaBS J0211+ 1051	10.8600	32.8050	1.46	3.63	VERITAS
15	PKS 2032+ 107	11.0000	308.8600	1.47	3.63	VERITAS
16	PG 1553+ 113	11.1900	238.9292	1.47	3.16	BOTH
17	RGB 0847+ 115	11.56389	131.8038	1.48	3.16	MAGIC
18	CTA 102	11.7310	338.1520	1.48	3.63	VERITAS
19	BL 1722+ 119	11.8708	261.2679	1.49	3.16	MAGIC
20	1ES 1440+ 122	12.0111	220.7010	1.49	3.63	VERITAS
21	M87	12.3975	187.6970	1.50	3.63	VERITAS
22	PKS 0528+ 134	13.5320	82.7350	1.53	3.63	VERITAS
23	4C 14.23	14.4200	111.3200	1.55	3.63	VERITAS
24	RGB 0648+ 151	15.2736	102.1983	1.57	3.16	BOTH
25	4c15.54	15.8594	241.7775	1.58	3.16	MAGIC
26	3C 454.3	16.1480	343.4910	1.59	3.63	VERITAS
27	AO 0235+ 164	16.6164	39.6621	1.60	3.16	BOTH
28	RGB 0250+ 172	17.2025	42.6579	1.61	3.16	MAGIC
29	PKS 0735+ 178	17.7053	114.5308	1.62	3.16	MAGIC
30	OX 169	17.7300	325.8980	1.63	3.63	VERITAS
31	PKS 1717+ 177	17.7517	259.8042	1.63	3.16	BOTH
32	HB89 0317+ 185	18.7594	49.9658	1.65	3.16	BOTH
33	MG2 J071354+ 1934	19.5830	108.4820	1.67	3.63	VERITAS
34	1ES 1741+ 196	19.5858	265.9908	1.67	3.16	BOTH
35	OJ 287	20.1108	133.7033	1.68	3.16	BOTH
36	RGB 1117+ 202	20.2356	169.2758	1.68	3.16	MAGIC
37	1ES 0229+ 200	20.2881	38.2025	1.68	3.16	BOTH

38	RGB 0521+ 211	21.2142	80.4412	1.71	3.16	BOTH
39	PKS1222+ 21	21.3794	186.2270	1.71	3.16	BOTH
40	Crab Pulsar	22.0140	83.6330	1.73	3.63	VERITAS
41	RGB 0909+ 231	23.1867	137.2529	1.75	3.16	MAGIC
42	RGB 0321+ 236	23.6031	50.5000	1.76	3.16	MAGIC
43	PG 1424+ 240	23.8000	216.7517	1.77	3.16	BOTH
44	1ES 1255+ 244	24.2111	194.3829	1.77	3.16	MAGIC
45	0827+ 243	24.2200	127.4900	1.77	3.63	VERITAS
46	1ES 0647+ 250	25.0500	102.6938	1.79	3.16	MAGIC
47	RGB 1417+ 257	25.7236	214.4858	1.80	3.16	MAGIC
48	W Comae	28.2331	185.3821	1.86	3.16	BOTH
49	Ton 599	29.2460	179.8830	1.88	3.63	VERITAS
50	HB89 0912+ 293	29.5567	138.9683	1.89	3.16	MAGIC
51	ON 325	30.1169	184.4671	1.90	3.16	BOTH
52	1ES 1218+ 304	30.1769	185.3413	1.90	3.16	BOTH
53	B2 1520+ 31	31.7370	230.5420	1.94	3.63	VERITAS
54	4C 31.03	32.1380	18.2100	1.95	3.63	VERITAS
55	CGRaBS J1848+ 3219	32.3170	282.0920	1.95	3.63	VERITAS
56	B2 0619+ 33	33.4360	95.7180	1.97	3.63	VERITAS
57	HB89 1721+ 343	34.2994	260.8367	1.99	3.16	MAGIC
58	1ES 0120+ 340	34.3472	20.7867	1.99	3.16	MAGIC
59	B2 2308+ 34	34.4200	347.7720	1.99	3.63	VERITAS
60	RGB 0706+ 377	37.7433	106.6321	2.06	3.16	MAGIC
61	NVSS 232914+ 3754	37.9042	352.309167	2.06	3.16	MAGIC
62	1633+ 382	38.1350	248.8150	2.06	3.63	VERITAS
63	Mkn 421	38.2089	166.1138	2.07	3.16	BOTH
64	B3 2247+ 381	38.4103	342.5238	2.07	3.16	BOTH
65	RGB 0136+ 391	39.1000	24.1363	2.08	3.16	MAGIC
66	0FGL J1641.4+ 3939	39.6660	250.3550	2.09	3.63	VERITAS
67	Mkn 501	39.7603	253.4675	2.10	3.16	BOTH
68	IC 310	41.3247	49.1792	2.12	3.63	VERITAS
69	TeV J2032+ 4130	41.5100	308.0830	2.13	3.63	VERITAS
70	NGC1275	41.5117	49.9504	2.13	3.16	BOTH
71	1ES 2321+ 419	42.1831	350.9671	2.14	3.16	BOTH
72	BL Lac	42.2778	330.6804	2.14	3.16	BOTH
73	B3 0814+ 425	42.3800	124.5500	2.14	3.63	VERITAS
74	1ES 1426+ 428	42.6725	217.1358	2.15	3.16	BOTH
75	3C66A	43.0356	35.6650	2.16	3.16	BOTH
76	B3 1307+ 433	43.0847	197.3563	2.16	3.16	MAGIC
77	B3 1708+ 433	43.3120	257.4210	2.16	3.63	VERITAS
78	MG4J200112+ 4352	43.8814	300.3038	2.17	3.16	BOTH
79	B3 1343+ 451	44.8830	206.3880	2.19	3.63	VERITAS
80	GB6 B1310+ 4844	48.4750	198.1810	2.25	3.63	VERITAS

81	1ES 1011+ 496	49.4336	153.7675	2.26	3.16	BOTH
82	1150+ 497	49.5190	178.3520	2.27	3.63	VERITAS
83	1ES 0927+ 500	49.8406	142.6567	2.27	3.16	MAGIC
84	BL 1ZW187	50.2194	262.0775	2.28	3.16	MAGIC
85	1ES 1028+ 511	50.8933	157.8271	2.28	3.16	MAGIC
86	1ES 2344+ 514	51.7050	356.7700	2.30	3.16	BOTH
87	1ES 0806+ 524	52.3000	122.4542	2.31	3.16	BOTH
88	BZU J0742+ 5444	54.7400	115.6660	2.34	3.63	VERITAS
89	4C55.17	55.3828	149.4092	2.35	3.16	MAGIC
90	RGB 1903+ 556	55.6772	285.7983	2.36	3.16	MAGIC
91	RGB 1058+ 564	56.4697	164.6570	2.37	3.16	BOTH
92	RBS 1409	56.6569	219.2404	2.37	3.16	MAGIC
93	PG 1246+ 586	58.3414	192.0783	2.39	3.16	MAGIC
94	exo 0706+ 5913	59.1389	107.6250	2.40	3.16	BOTH
95	1ES 0033+ 595	59.8347	8.9692	2.41	3.16	MAGIC
96	S4 1030+ 61	60.8520	158.4640	2.42	3.63	VERITAS
97	RGB 0505+ 612	61.2267	76.4950	2.43	3.16	MAGIC
98	LSI + 61 303	61.2290	40.1310	2.43	3.63	VERITAS
99	1ES 1959+ 650	65.1486	299.9992	2.47	3.16	BOTH
100	S4 0954+ 658	65.5653	149.6967	2.48	3.16	MAGIC
101	CGRaBS J1849+ 6705	67.0950	282.3170	2.49	3.63	VERITAS
102	RGB 1136+ 676	67.6178	174.1254	2.49	3.16	MAGIC
103	1ES 0502+ 675	67.6233	76.9842	2.49	3.16	BOTH
104	GB6 J1700+ 6830	68.5020	255.0390	2.50	3.63	VERITAS
105	HB89 1749+ 701	70.09750	267.1367	2.52	3.16	BOTH
106	Mkn 180	70.1575	174.1100	2.52	3.16	BOTH
107	S5 0836+ 71	70.8950	130.3520	2.52	3.63	VERITAS
108	S5 0716+ 714	71.3433	110.4725	2.53	3.16	BOTH
109	S5 1803+ 78	78.4680	270.1900	2.57	3.63	VERITAS

Table 6: List of sources used by NToO from November 2013 to December 2015. In the table the source name, the declination (DEC), the right ascension (RA), search bin radius, and threshold for sending alerts is listed. The last column indicates if the source belongs only to the MAGIC list or VERITAS list or if the source is present in the list for both experiments (BOTH).

L.P.	Source	DEC (deg)	RA (deg)	Search radius (deg)	Threshold (σ)	Exper.
1	PG 1553+113	11.1902	238.9418	1.47	3.16	BOTH
2	PKS 1424+240	23.9750	216.7597	1.77	3.16	BOTH
3	PKS 1717+177	17.7425	259.8300	1.63	3.16	BOTH

4	RBS 0413	18.8266	49.9094	1.65	3.16	BOTH
5	RBS 0958	20.2269	169.3050	1.68	3.16	MAGIC
6	RX J0805.4+7534	75.5878	121.3421	2.56	3.16	MAGIC
7	S5 0716+71	71.3496	110.4757	2.53	3.16	BOTH
8	TXS 1055+567	56.48010	164.6656	2.37	3.16	BOTH
9	W Comae	28.2391	185.3740	1.86	3.16	BOTH
10	1ES 1215+303	30.1093	184.4672	1.90	3.16	BOTH
11	1ES 1959+650	65.1572	300.0204	2.47	3.16	BOTH
12	1ES 2321+419	42.2001	350.9539	2.14	3.16	BOTH
13	3C 66A	43.0358	35.6617	2.16	3.16	BOTH
14	GB6 J1542+6129	61.4887	235.7294	2.43	3.16	MAGIC
15	GB6 J1838+4802	47.9939	279.6958	2.24	3.16	MAGIC
16	MS 1458.8+2249	22.6388	225.2749	1.74	3.16	MAGIC
17	Mkn 421	38.2134	166.1199	2.07	3.16	BOTH
18	Mkn 501	39.7631	253.4814	2.10	3.16	BOTH
19	PMN J0948+0022	0.3740	147.2390	1.21	3.63	VERITAS
20	BL 0414+009	1.0900	64.2188	1.23	3.63	VERITAS
21	PKS B0906+015	1.3600	137.2920	1.23	3.63	VERITAS
22	RGB J0152+017	1.7779	28.1396	1.24	3.63	VERITAS
23	3C 273	2.0525	187.2779	1.25	3.63	VERITAS
24	MG1 J050533+0415	4.2650	76.3950	1.30	3.63	VERITAS
25	J123939+044409	4.7000	189.9000	1.31	3.63	VERITAS
26	HESS J0632+057	5.8056	98.2429	1.34	3.63	VERITAS
27	4C +09.57	9.6300	267.8900	1.43	3.63	VERITAS
28	PKS 0754+100	9.9400	119.3100	1.44	3.63	VERITAS
29	PKS 1502+106	10.4940	226.1040	1.45	3.63	VERITAS
30	CGRaBS J0211+1051	10.8600	32.8050	1.47	3.63	VERITAS
31	PKS 2032+107	11.0000	308.8600	1.47	3.63	VERITAS
32	CTA 102	11.7310	338.1520	1.48	3.63	VERITAS
33	1ES 1440+122	12.0111	220.7010	1.49	3.63	VERITAS
34	M 87	12.3975	187.6970	1.50	3.63	VERITAS
35	PKS 0528+134	13.5320	82.7350	1.53	3.63	VERITAS
36	4C 14.23	14.4200	111.3200	1.55	3.63	VERITAS
37	RGB 0648+151	15.2736	102.1983	1.57	3.63	VERITAS
38	3C 454.3	16.1480	343.4910	1.59	3.63	VERITAS
39	AO 0235+164	16.616	39.6621	1.60	3.63	VERITAS
40	OX 169	17.7300	325.8980	1.63	3.63	VERITAS
41	MG2 J071354+1934	19.5830	108.4820	1.67	3.63	VERITAS
42	1ES 1741+196	19.5858	265.9908	1.67	3.63	VERITAS
43	OJ 287	20.1108	133.7033	1.68	3.63	VERITAS
44	1ES 0229+200	20.2881	38.2025	1.69	3.63	VERITAS
45	RGB 0521+211	21.2142	80.4413	1.71	3.63	VERITAS
46	PKS1222+21	21.3794	186.2271	1.71	3.63	VERITAS

47	Crab Pulsar	22.0140	83.6330	1.72	3.63	VERITAS
48	0827+243	24.2200	127.4900	1.77	3.63	VERITAS
49	Ton 599	29.2460	179.8830	1.88	3.63	VERITAS
50	1ES 1218+304	30.1769	185.3413	1.90	3.63	VERITAS
51	B2 1520+31	31.7370	230.5420	1.94	3.63	VERITAS
52	4C 31.03	32.1380	18.2100	1.94	3.63	VERITAS
53	CGRaBS J1848+3219	32.3170	282.0920	1.95	3.63	VERITAS
54	B2 0619+33	33.4360	95.7180	1.97	3.63	VERITAS
55	B2 2308+34	34.4200	347.7720	1.99	3.63	VERITAS
56	1633+382	38.1350	248.8150	2.06	3.63	VERITAS
57	B3 2247+381	38.4103	342.5238	2.07	3.63	VERITAS
58	0FGL J1641.4+3939	39.6660	250.3550	2.09	3.63	VERITAS
59	IC 310	41.3247	49.1792	2.12	3.63	VERITAS
60	TeV J2032+4130	41.5100	308.0830	2.13	3.63	VERITAS
61	NGC1275	41.5117	49.9504	2.13	3.63	VERITAS
62	BLLac	42.2778	330.6804	2.14	3.63	VERITAS
63	B3 0814+425	42.3800	124.5500	2.14	3.63	VERITAS
64	1ES 1426+428	42.6725	217.1358	2.15	3.63	VERITAS
65	B3 1708+433	43.3120	257.4210	2.16	3.63	VERITAS
66	MG4J200112+4352	43.8814	300.3038	2.17	3.63	VERITAS
67	B3 1343+451	44.8830	206.3880	2.19	3.63	VERITAS
68	GB6 B1310+4844	48.4750	198.1810	2.25	3.63	VERITAS
69	1ES 1011+496	49.4336	153.7675	2.26	3.63	VERITAS
70	1150+497	49.5190	178.3520	2.26	3.63	VERITAS
71	1ES 2344+514	51.7050	356.7700	2.30	3.63	VERITAS
72	1ES 0806+524	52.3000	122.4542	2.31	3.63	VERITAS
73	BZU J0742+5444	54.7400	115.6660	2.34	3.63	VERITAS
74	exo 0706+5913	59.1389	107.6250	2.40	3.63	VERITAS
75	S4 1030+61	60.8520	158.4640	2.42	3.63	VERITAS
76	LSI +61 303	61.2290	40.1310	2.43	3.63	VERITAS
77	CGRaBS J1849+6705	67.0950	282.3170	2.49	3.63	VERITAS
78	1ES 0502+675	67.6233	76.9842	2.49	3.63	VERITAS
79	GB6 J1700+6830	68.5020	255.0390	2.50	3.63	VERITAS
80	HB89 1749+701	70.0975	267.1367	2.52	3.63	VERITAS
81	Mkn 180	70.1575	174.1100	2.52	3.63	VERITAS
82	S5 0836+71	70.8950	130.3520	2.52	3.63	VERITAS
83	S5 1803+78	78.4680	270.1900	2.57	3.63	VERITAS

Table 7: List of sources used by NToO for IC-2013 and IC-2014 season.